Numerical modeling of surf zone dynamics under weakly plunging breakers with SPH method

CrossMark

Christos V. Makris [a,*], Constantine D. Memos [b], Yannis N. Krestenitis [a]

[a] Department of Civil Engineering, Faculty of Engineering, Aristotle University of Thessaloniki (AUTh), 54124 Thessaloniki, Greece
[b] School of Civil Engineering, National Technical University of Athens (NTUA), Heroon Polytechniou 5, Zografos, 15780 Athens, Greece

ARTICLE INFO

ABSTRACT

The wave breaking of weak plungers over a relatively mild slope is investigated in this paper. Numerical modeling aspects are studied, concerning the propagation and breaking of shore-normal, nonlinear and regular waves. The two-dimensional (2-D) kinematics and dynamics (fluctuating flow features and large 2-D eddies) of the wave-induced flow on a vertical cross-section over the entire surf zone are simulated with the use of Smoothed Particle Hydrodynamics (SPH). The academic 'open source' code SPHysics v.2 is employed and the viscosity treatment is based on a Sub-Particle Scale (SPS) approach, similarly to the Large Eddy Simulations (LES) concept. Thorough analysis of the turbulent flow scales determines the necessary refinement of the spatial resolution. The initial particle discretization reaches down to the demarcation point between integral turbulence length scales and Taylor micro-scales. A convolution-type integration method is implemented for the transformation of scattered Lagrangian particle data to Eulerian values at fixed gauges. A heuristic technique of ensemble-averaging is used for the discrimination of the fluctuating flow components from coherent structures and ordered wave motion. Comparisons between numerical and experimental data give encouraging results for several wave features. The wave-induced mean flows are simulated plausibly, and even the 'streaming' effect near the bed is reproduced. The recurring vorticity patterns are derived, and coherent 2-D structures inside the surf zone are identified. Fourier spectral analysis of velocities reveals isotropy of 2-D fluctuating dynamics up to rather high frequencies in shear intensified regions. The simulated Reynolds stresses follow patterns that define the characteristic mechanism of wave breaking for weak plungers. Persisting discrepancies at the incipient breaking region confirm the need for fine, massively 'parallel' 3-D SPS-SPH simulations.

© 2015 Elsevier Ltd. All rights reserved.

1. Introduction

Near-shore wave propagation, shoaling, and breaking are three of the most significant coastal processes. In particular, depth related wave breaking is of major importance in assessing the surf and swash zone dynamics. Research, covering the subject, has since long focused on the evolution of the near-shore wave patterns, the detailed reproduction of the free surface deformations and the wave-induced kinematics. Despite that, the underlying hydrodynamics, which describe the respective processes, are far from completely elucidated. Thus, coastal engineers and scientists nowadays are involved in the analysis of the extremely complex hydrodynamic field in the surf zone. Specifically they are concerned, among other issues, with a 'clean' definition of turbulent characteristics and a consequent proper averaging method for near-shore features. In this way, they aim for a robust

definition of coherent turbulent structures and ways to identify intermittent turbulent events, which primarily control sediment movements in cross-shore morphodynamic evolution of the surf zone. In this direction, past research has concentrated on the derivation of instantaneous and phase-averaged values of hydrodynamic quantities and fluid properties. Such features are the free surface elevation η, the vorticity ω, the turbulent components of velocities u', v' and w' (i.e. $u = \bar{u} + u'$, u is the horizontal streamwise fluid velocity and $\bar{u}$ its averaged value), the turbulent kinetic energy (TKE) $k = (u'^2 + v'^2 + w'^2)/2$, the turbulent shear and normal stresses $\tau_{ss} = -\rho u'w'$ and $\tau_{nx} = \rho u'^2$, $\tau_{ny} = \rho v'^2$, $\tau_{nz} = \rho w'^2$ respectively (ρ is the fluid density), the topology of vortical patterns, the characteristic turbulence length and time scales etc. Moreover, the conceptual design of modern coastal protection works requires nowadays the calculation of wave-induced mean flows, wave set-up, run-up and overtopping, not properly provided by classical analytical theories or traditional numerical wave models. Quantification of the aforementioned features and processes has been extensively provided throughout the last decades by various laboratory experiments, which involve physical modeling of wave

generation, propagation, and breaking of the spilling or plunging type on beach slopes placed inside wave flumes. These efforts are numerous and mostly account for linear and nonlinear regular and solitary waves. Thorough reviews on surf and swash zone dynamics and turbulence can be found in the works of Elfrink and Baldock (2002), Longo et al. (2002), and Christensen (2006).

1.1. Typical experiments for plunging breakers

The experimental methods implemented, vary from the early photographic capturing of the breaking wave process, with simultaneous measurements of the free surface at specific gauge points, to the more elaborate Acoustic/Laser Doppler Velocimetry (ADV/LDV) or Anemometry (LDA), as those used by Nadaoka et al. (1989). One of the most classic series of experiments with LDA technique is that of Ting and Kirby (1994, 1995), investigating the dynamics of plunging breaking waves. They studied turbulence transport and undertow velocities in detail, by determining the time-mean and the variation of local phase-averaged 2-D TKE together with the time- and phase-averaged horizontal turbulent velocities. Moreover phase-averaged η, u and w were derived, as well as turbulence production terms. Interestingly, the cross-shore sediment transport was proved to follow a shoreward direction for plunging breakers. Li and Dalrymple (1998) verified, through ADV measurements, that the steady undertow created by wave breaking over a sloping bed slowly flows seaward, becomes unstable and creates a migrating submerged vortex train with shorter length scales and longer time scales than the incident waves. These vortices rotate about horizontal axes parallel to the shoreline. Moreover they showed that undertow instabilities lead the wave-averaged vortices to rotate in the same direction as the wave-induced water particle trajectories near the water surface, and in the opposite direction at about mid-depth. Petti and Longo (2001) conducted time series analysis of periodic signals of u, w with the use of a LDV system, along several vertical gauge sections in the swash zone. Their goals were to describe the wave front dynamics, calculate the length and velocity macro- and micro-scales and define the Eulerian frequency spectrum, which finally revealed a double structure. Longo (2003) additionally analyzed k measurements using a discrete wavelets method, computed and phase resolved the different scale vortices. The author concluded that the dominant vortices are of micro- and mid-size carrying the 70% of total turbulent energy under wave crest. Another significant endeavor, implementing the LDA method, was that by Stansby and Feng (2005). They used a large number of gauges, in order to investigate thoroughly the kinematics of the surf zone created by weakly plunging breakers. They aimed at the determination, through ensemble-averaging, of recurrent vertical flow structures, including from large-scale motions down to small-scale eddies. The coherent character of multiple 2-D vortical structures was confirmed, specifically just before and at the onset of breaking, leading to elongated ones near and along the free surface during the turbulent bore propagation. Period-averaged ω, u' and w' were also obtained showing onshore mass transport above trough level and undertow-type backflow below it. Thick vorticity layers were observed at trough level and a thin one rotating oppositely near the bottom solid boundary. Various turbulence terms were also evaluated. Conclusively, physical modeling has set the grounds of profound insight on the matter, yet laboratory experiments are quite expensive and relate always to strict hydraulic and inflexible geometric conditions.

1.2. Numerical simulations of plunging wave breaking

Classic wave models (Boussinesq-type etc.) give satisfactory simulation results near-shore, mostly accounting for spilling type breakers, while their predictability depends on the wave breaking formulation, e.g. surface roller or eddy viscosity model. Modern approaches comprise of elaborate Computational Fluid Dynamics (CFD)

techniques, modeling the Navier–Stokes (N-S) equations on a grid or mesh. The most prominent are the models solving the Reynolds Averaged Navier Stokes (RANS) equations, usually combined with surface tracking techniques like Volume-of-Fluid (VOF) method; the Large Eddy Simulations (LES) with Sub-Grid Scale (SGS) approaches for the closure of turbulence; the computationally very expensive Direct Numerical Simulations (DNS) etc.

In this framework, Bradford (2000) presented an incompressible N-S/VOF model to examine the accuracy of the numerical approximations of breaker location, wave height, undertow, and k. Velocity fields and kinetic energy contours under plunging breakers were presented, without description of the vorticity patterns of the flow. Christensen and Deigaard (2001) described turbulence by LES through a SGS Smagorinsky-type model for the small unresolved scales and depicted complicated flow phenomena such as obliquely descending eddies (ODE), reported by Nadaoka et al. (1989). A complete numerical study was performed by Watanabe and Saeki (2002), in which the vorticity of 2-D coherent structures and large-scale eddies was investigated. Moreover, spatial gradients in frequency spectra of kinetic energy and enstrophy were associated with Reynolds stress production, transport and dissipation at various turbulent mixing length scales. Mean velocity field, wave and turbulent kinetic energy in the surf zone were also evaluated. Zhao et al. (2004) created a 2-D model with moderate computer requirements using VOF combined with a log-law mean velocity profile for the bottom boundary and deriving η, u, w, wave heights, and undertow profiles. Their SGS turbulent transport mechanism revealed order similarities between turbulent production and dissipation. The first was primarily located at the wave front and above the wave trough, whereas the second hindward of the waves. At the trough level, 2-D turbulence was being equally convected and diffused, yet above it, domination of turbulent convection was obvious. The dissipation of 2-D TKE k in the spilling breaker case continued during bore propagation and became very rapid under the plunging breaker with time scales of less than one wave period. Watanabe et al. (2005) proposed a 3-D LES model with SGS to study the instabilities of vorticity in the saddle region of strain between the rebounding jet of the breaker and the spanwise vortex. This led to undular motions amplified on a braid-type structure. The resulting vortex loop defined an envelope region surrounding the adjacent vortices forming a rib-like formation similarly to ODE. Christensen (2006) implemented the N-S/VOF concept together with either an SGS or a k-equation model for the turbulence scales and calculated the wave set-up, the undertow and turbulence features for a rather coarse computational resolution. An overall overprediction of turbulence levels was found because of the use of standard values of model parameters. Vortical structures were observed around both the vertical and transverse axes, yet the elongated cross-shore turbulent structures were dominant. Bakhtyar et al. (2009) used a k-ε (ε: dissipation of k) model for turbulence closure in combination with a 2-D RANS-VOF method, presenting plausible results in the surf zone except near the breaking point, and excellent ones in the swash zone.

1.3. Review of SPH literature on wave breaking

All of the above methods are associated to mesh-based numerical models. On the other hand, mesh-free methods are also more and more implemented nowadays for the numerical simulation of wave breaking and surf zone turbulence. Smoothed Particle Hydrodynamics (SPH) (Monaghan, 1992, 2005) is the most widely discerned particle method, that stands out as a promising modern technique in dealing with highly deformed free surface flows (FSFs), e.g. plunging wave breakers, using Lagrangian formulation without the strenuous use of a toggling computational grid or mesh. In recent literature, the results of SPH simulations for plunging wave breaking were visually impressive (Gómez-Gesteira et al., 2010b; Dalrymple and Rogers, 2006), yet

somehow display lack of thorough affirmation concerning detailed turbulent flow features.

Shao and Ji (2006) used a LES-type SPH approach, i.e. a Sub-Particle Scale (SPS) turbulence closure model (Gotoh et al., 2001; Shao and Gotoh, 2005), to produce notable results, yet only for free surface displacements, plunging jet topology and turbulent intensities. Khayyer et al. (2008) studied thoroughly the geometrical characteristics of a plunging breaker for the case of a solitary wave, while proposing a Corrected Incompressible SPH (CISPH) method, based on a variational approach, for accurate tracking of the water surface (see further analysis in Section 2.1.). Numerical data agreed with experimental ones for wave heights and velocities of the plunging jet tip. Khayyer et al. (2009) took this approach even further by proposing new criteria for the derivation and employment of a high-order source term based on more accurate differentiation, in order to reproduce more accurate pressure fields with SPH and tackle the respective inherent problem of the method. The plunging event was in their case induced by the reversed flow of a water jet after an impact of a dam break on a solid vertical barrier. Shao (2010) presented an ISPH method to simulate wave interactions with porous media (bed and breakwater), by including additional frictional forces into the SPH equations. The model was validated for solitary and regular waves, and comparisons were good for pressures (against other models' data), water profiles (against experimental data) and reasonable for flow velocities. Gotoh et al. (2014) presented two enhancement schemes (Higher order Laplacian: HL; Error-Compensating Source: ECS) of Poisson pressure equation in ISPH for the simulation of the sloshing problem and related impact forces. They provided good qualitative comparisons for the plunging jet reproduction and quantitative ones for pressures. The plunger was yet again associated with a water jet of the return flow after the impact of a dam break in a sloshing tank.

Other interesting recent studies of water-body interactions are those by Skillen et al. (2013) in 2-D and Wei et al. (2015) in 3-D; they both present validation of their SPH models in terms of water levels and velocities and give useful results about the flow field in the vicinity of the interacting solids. Farahani and Dalrymple (2014) studied the turbulent vortical structures under breaking solitary waves with the use of 3-D SPH, the numerical results of which compared very well against experimental data in terms of water surface evolution and horizontal velocities. The authors numerically detected coherent turbulent structures, organized in space and time, in the form of reversed horseshoe (hairpin) vortices submersing downward behind a spilling breaker. The newly found counter rotating legs of the reversed horseshoe structures were identified as the continuation of the classic ODE. These structures were related to sweep events of turbulence that transported momentum and TKE towards the bed, through a downwelling motion, with the vortex turning mechanism distinguishable among others. The authors did not detect similar coherent flow patterns for the case of a solitary wave breaking in plunging form. Hence, rigorous validation of SPH simulation results against reliable experimental data on plunging breaking for regular wave trains is imperative.

Therefore, in the present paper, we provide refined SPS-SPH numerical simulations of regular nonlinear waves breaking in weakly plunging form, with the use of the SPHysics open-source code (Gómez-Gesteira et al., 2012). All past SPH wave breaking simulations dealt with strong plungers. The latter usually create water jets which are more likely to penetrate the free surface in the area they impinge and consequently produce large amounts of vertically distributed turbulence. During the breaking of weak plungers, however, the jet is almost totally reflected when it makes contact with the forward wave trough. The jet rebounds and splashes several times, while it generates horizontal stretching of relative eddies and vortical structures (Christensen and Deigaard, 2001).

1.4. Aims of the study

The calibration and affirmation of a state-of-the-art SPH implementation to predict the details of the entire wave breaking process, under the said conditions, ensued as a major goal of the research presented below. Conclusively our aim was to provide an accurate simulation of the highly nonlinear process of wave breaking specifically for shore-normal weak plungers on a plane and relatively mild impermeable slope. Extensive comparative analysis between model and experimental results is presented here, shedding light to the robustness of the SPH method and indicating specific upgrades for future research. We focus on good comparisons of wave heights, time- and ensemble-averaged u, w and η distributions, wave set-up, crest and trough envelopes against experimental data. The 2-D turbulent flow features are also produced, such as recurring vorticity patterns, coherent structures, u' and w' Fourier spectra, and vertical mapping of the Reynolds stresses. The analysis shows isotropic behavior of the fluctuating hydrodynamic components up to rather high frequency spectral bands. The simulation of wave-induced mean flows plausibly reproduced phenomena not well traced in the past literature on numerical wave breaking.

2. Numerical method

SPH is one of the most ingenuous modern numerical methods for the simulation of hydrodynamic FSFs (Monaghan, 1994, 2005). It is a mesh-free particle method, implementing Lagrange-type approximation for N-S equations, through integral interpolation smoothing functions. Its Lagrangian nature allows the unhindered simulation of FSFs with strong deformations, such as wave breaking (e.g. plunging) or wave-structure interaction in coastal areas, as described by Rogers and Dalrymple (2004), Dalrymple and Rogers (2006) and Crespo et al. (2007, 2008). Thorough analysis of SPH can be found in the books of Liu and Liu (2003) and Violeau (2012), thus only general reference of the constitutive equations and assumptions used is given here.

2.1. SPH basic features

The method's fundamental principle is the integral interpolation of any given (scalar or vectorial) function $A(\mathbf{r})$ in the computational domain that reads:

$$A(\mathbf{r}) = \int A_j(\mathbf{r}')W(\mathbf{r} - \mathbf{r}', h)d\mathbf{r}' \qquad (1)$$

where $h = c_f \cdot [(dx)^2 + (dz)^2]^{1/2}$ is the smoothing length (for 2-D), dx and dz is the horizontal and vertical spatial discretization respectively, c_f is a smoothing calibration parameter, $\mathbf{r}$ and $\mathbf{r}'$ are the arbitrary particle point location and the distance between particles respectively, and $W(\mathbf{r}, h)$ is the distance varied weighting function called kernel. Please note that the vector and tensor quantities are presented in bold font. For an arbitrary particle i, Eq. (1) and the derivative of $A(\mathbf{r})$ read in discretized notation:

$$A_i(\mathbf{r}) = \sum_j A_j \left(\frac{m_j}{\rho_j} \right) W_{ij} \; \Rightarrow \; \nabla A_i = \sum_j A_j \left(\frac{m_j}{\rho_j} \right) \nabla_i W_{ij} \qquad (2)$$

where m_j and ρ_j are the mass and the density of any particle j and W_{ij} is the kernel in particle notation. The summation is over all the particles j within the region of compact support of the kernel function for an arbitrary particle i (Gómez-Gesteira et al., 2010b).

A variety of bell-shaped weighting functions is available in the bibliography, all accounting for certain attributes, such as positivity, compact support, normalization, monotonic decreasing and delta function behavior (for infinitely small h). Two of the classic ones, used in most of our simulations, are the cubic spline and the

quintic Wendland (1995) kernels, given respectively by:

$$W(r_{ij}, h) = a_D \begin{cases} 1 - \dfrac{3}{2}q^2 + \dfrac{3}{4}q^3 & 0 \le q \le 1 \\ \dfrac{1}{4}(2-q)^3 & 1 < q \le 2 \quad (cubic\ spline) \\ 0 & q > 2 \end{cases}$$

and

$$W(r_{ij}, h) = a_D \begin{cases} \left(1 - \dfrac{q}{2}\right)^4 (1 + 2q) & 0 \le q \le 2 \\ 0 & q > 2 \end{cases} \quad (Wendland)$$

(3)

where q is r_{ij}/h, α_D is $10/(7\pi h^2)$ and $7/(4\pi h^2)$ respectively in 2-D, r_{ij} is the distance between particles i and j. In practice the kernel influence domain is confined in a radial distance of $2h$. A tracking technique like 'nearest neighbor list' is used to truncate the summation in Eq. (2), thus taking into account only the neighbor particles close to the integration point.

Conservation of mass (continuity) and momentum equations (N-S) are written according to Monaghan (1994) in particle formulation as:

$$\frac{d\rho_i}{dt} = \sum_j m_j \left(\mathbf{u}_i - \mathbf{u}_j\right) \cdot \nabla_i W_{ij}$$

(4)

$$\frac{d\mathbf{u}_i}{dt} = -\sum_j m_j \left(\frac{\mathbf{P}_i}{\rho_i{}^2} + \frac{\mathbf{P}_j}{\rho_j{}^2}\right) \cdot \nabla_i W_{ij} + \mathbf{g}$$
$$+ \sum_j m_j \left(\frac{4\nu \mathbf{r}_{ij} \nabla_i W_{ij}}{(\rho_i + \rho_j)|\mathbf{r}_{ij}|^2}\right) \mathbf{u}_{ij}$$

(5)

where $\mathbf{u}_i$ is the velocity of particle i and $\mathbf{u}_{ij} = \mathbf{u}_i - \mathbf{u}_j$, $\mathbf{P}_i$ and $\mathbf{P}_j$ are the pressures of particles i and j respectively, m_i is the mass and ρ_i the density of particle i, $\mathbf{g} = (0,0,9.81)$ m/s^2 is the gravitational acceleration vector, ν is the kinematic viscosity of water taken here equal to 10^{-6} m^2/s, and W_{ij} is the kernel relating particle i to arbitrary surrounding ones j within its influence domain.

The momentum conservation properties of the classic equation of motion in SPH (Eq. (5); see also Eq. (12) in Section 2.3.1.) are discussed thoroughly by Khayyer et al. (2008) in their analysis of the CISPH method, used for accurate tracking of water surface in breaking waves. They derived corrective terms, based on a variational approach, to ensure the preservation of angular momentum in ISPH formulations. They highlighted that inter-particle forces due to pressure (first summation term in the right-hand side of Eq. (5)) are radial and anti-symmetric, but this is not the case for viscous forces (last term in the right-hand side of Eq. (5)). They proved that the total sum of all interaction pairs between particles, due to pressure gradient and the viscosity term, will vanish and total linear momentum of the system will be preserved; evidence of that is given in Eqs. A3–A6 and Fig. A(2) of the Appendix in Khayyer et al. (2008). They observed that the angular moment of the two interacting forces between a pair of particles depends on the isotropy of the internal stress tensor. Due to the anisotropic nature of the viscous stresses in realistic viscosity calculations, such as in ISPH and SPS-SPH, the resulting viscous forces are not collinear with the position vector $\mathbf{r}_{ij}$ and could give an extra moment. This could lead to a non-zero summation of all the moments between each pair of particles, and therefore angular momentum might not be conserved. Their CISPH method tries to ensure correct calculation of viscous accelerations and bend the problem.

Particles are manipulated to move with approximately the average velocity of their neighbors, preventing them from occupying the same location with time. This is accomplished with the use of the following kinematic relation, called XSPH correction (Monaghan, 1989):

$$\frac{d\mathbf{r}_i}{dt} = \mathbf{u}_i + \varepsilon_e \sum_j m_j \left(\frac{\mathbf{u}_i - \mathbf{u}_j}{\bar{\rho}_i}\right) W_{ij}$$

(6)

where average particle density $\bar{\rho}_i = (\rho_i + \rho_j)/2$ and $\varepsilon_e \approx 0.5$ is an empirical factor. However, the XSPH scheme is known to usually lead to non-physical oscillations in the pressure and density fields, especially when simulating incompressible flow problems, as shown by Fatehi and Manzari (2011). Specifically, when solving the mass conservation equation in standard Weakly Compressible SPH (WCSPH; see below), the XSPH approach may cause numerical dispersion in the form of tensile instability and sometimes divergence, originating from the form of spatial discretization used for the pressure term. Moreover XSPH could induce somewhat inaccurate results in the case of flows with sharp velocity gradients (Shahriari et al., 2012). However, the latter was confirmed for flows in closed conduits (cardiovascular flow in biomedics) with the presence of oblong barrier obstacles.

Monaghan (2005) highlighted the fact that the XSPH scheme does not conserve energy and proposed an implicit XSPH approach to resolve this issue, by re-applying the values $\mathbf{u}_i = d\mathbf{r}_i/dt$ and $\mathbf{u}_j = d\mathbf{r}_j/dt$ in the summation term of Eq. (6). Another remedy has been proposed by Fatehi and Manzari (2011), who suggested a modified approach that, in combination with the Wendland kernel, uses a different discretization scheme for the second derivative of the pressure field, based on the pressure–velocity decoupling problem associated with the so-called collocated grid methods. Alternatively, ISPH schemes with projection based pressure correction have been proposed and showed high accuracy and stability for internal flows, providing noise-free pressure fields in contrast to WCSPH (Xu et al., 2009). The method relied on particle shifting algorithms and was expanded for free surface flows, based upon Fick's law of diffusion (Lind et al., 2012), and allowed the redeployment of particles in order to prevent highly anisotropic distributions and numerical instability.

Furthermore the problem of particle inter-penetrations is not completely addressed by XSPH. Nonetheless, it has been minimized by the ECS scheme presented by Khayyer and Gotoh (2011) for the stabilization and enhancement of the performance of Moving Particle Semi-implicit (MPS) method, which is analogous to SPH. Modifications corresponded to a reformed source term of the Poisson pressure equation counterbalancing high-order errors with dynamic coefficients as functions of the instantaneous flow field, and the derivation of a corrective matrix, on the basis of Taylor series expansion, for a more accurate approximation of the pressure gradient. Tsuruta et al. (2013) proposed the Dynamic Stabilization (DS) scheme for any particle method (MPS, SPH etc.), and thus provided a way to adequately induce repulsive inter-particle forces, based on the instantaneous distribution of particles, in order to eliminate the inter-particle penetration problem, which is one of the main causes of instabilities in SPH.

In order to relate the pressure to the density of the fluid, the artificial compressibility concept is incorporated in (weakly) compressible SPH models (WCSPH approach), giving the advantage of using an equation of state instead of having to solve for an extra Poisson-type equation for pressure, which describes incompressible flows. Monaghan (1994), based on Batchelor (1974), provides the following expression for the particle pressure in WCSPH models:

$$P = B[(\rho/\rho_o)^\gamma - 1]$$

(7)

where $B = c_{s,o}{}^2 \rho_o/\gamma$, $\gamma = 7$, reference density is $\rho_o = 1000$ kgr/m^3 and $c_{s,o} = c(\rho_o) = \partial P/\partial \rho|_{\rho_o}$ is the speed of sound in water. To enhance stability of the combined WCSPH and XSPH approach and mitigate their aforementioned limitations for the reproduction of the violent free surface deformations in this study, the Shepard density averaging filter is also applied (see Eq. (13) in Section 2.3.1.)

2.2. SPHysics model

In order to verify the capability of state-of-the-art SPH to predict the details of the entire wave breaking process, the academic 'open source' numerical code SPHysics v.2 (Gómez-Gesteira et al., 2012) was used. It has been developed during the last years by

several researchers around the world with its origin at Johns Hopkins University (Baltimore, USA). Some of the crucial assumptions made in SPHysics are presented below.

In all the simulations presented here, solid boundaries inside the computational domain were treated as repulsive boundaries (Gómez-Gesteira et al., 2012). This boundary condition was introduced by Monaghan (1994) to ensure that fluid particles remain inside the computational domain and never penetrate solid boundaries. The particles that form boundaries impose centerline forces on water particles, similar to inter-molecular forces in the form given by the Lennard-Jones potential. A refined version of this assumption was presented by Monaghan and Kos (1999). They used an interpolation procedure, in order to minimize the interspacing effects of the solid particles on the boundary repulsive forces. We also followed this treatment, which defined a more or less slip boundary condition at the inviscid limit.

Several numerical schemes are available in the SPHysics code (Gómez-Gesteira et al., 2012). The symplectic time integration technique (Leimkuhler et al., 1996) was preferred in the present study, due to faster computational times. In general, the total energy was conserved within proposed limits (Monaghan, 1994), of 0.1% energy loss over 400 time steps, as stated by the original authors of the code. This accounted for 5–20 ms of wave propagation time per cycle. The time step Δt was variable (Monaghan and Kos, 1999), yet small enough to ensure the fulfillment of the Courant–Friedrichs–Lewy (CFL) condition, together with the force per unit mass $\mathbf{f}_i$ and the viscous diffusion terms criteria (Monaghan, 1989), based on:

$$\Delta t = 0.3 \cdot \min(\Delta t_f, \Delta t_{cv}),$$

$$\text{where} \begin{cases} \Delta t_f = \min_i(\sqrt{h/|\mathbf{f}_i|}) \\ \Delta t_{cv} = \min_i\left(h/\left(c_s + \max_j\left|h\mathbf{u}_{ij}\mathbf{r}_{ij}/\mathbf{r}_{ij}^2\right|\right)\right) \end{cases} \quad (8)$$

2.3. Viscosity treatment

Dalrymple and Rogers (2006) discussed the use of the artificial viscosity term (Monaghan, 1992), which is used to keep particles from interpenetration, represent viscosity and provide numerical stability for free surface problems. Nonetheless it influences negatively the shear in the fluid, by introducing very dissipative structures in the numerical scheme, a fact in particular significant if someone tries to describe coherent turbulent structures. In SPHysics an SPS turbulence closure model is available for the unresolved scales, while the large scale structures could be reproduced implicitly by the SPH model with proper spatial resolution.

2.3.1. Sub-particle scale turbulence closure

The SPS approach of modeling turbulence was described by Gotoh et al. (2001) to represent the effects of turbulence in their model. In the Appendix of the SPHysics User Guide (Gómez-Gesteira et al., 2010a) a concise description of the LES-SGS numerical model approach can be found (Gotoh et al., 2004). A Favre-averaging technique, $\bar{f} = \overline{\rho f}/\bar{\rho}$ where the overbar denotes flat-top arbitrary spatial filtering (Rogers and Dalrymple, 2004), was used for the compressible fluid, causing respective alterations to the governing momentum equation. An extra term accounting for internal friction effects, $(\nabla \cdot \tau^*/\bar{\rho})$, was introduced with discrete particle notation (Gómez-Gesteira et al., 2010a, 2012) in Eq. (5), involving the SPS stress tensor τ^* in the likes of LES-SGS models, with its elements written in Einstein notation:

$$\tau_{ij}^* = \bar{\rho}\left(2\nu_t\tilde{S}_{ij} - \frac{2}{3}\nu_t k_{SPS}\delta_{ij} - \frac{2}{3}C_I\Delta l^2\delta_{ij}\left|\tilde{S}_{ij}\right|^2\right) \quad (9)$$

where ν_t is the turbulent eddy viscosity, $C_I = 0.0066$ (Blin et al., 2002), Δl is the inter-particle spacing, δ_{ij} is the Kronecker delta, k_{SPS} is the SPS TKE, $|\tilde{S}_{ij}| = (2\tilde{S}_{ij}\tilde{S}_{ij})^{1/2}$ is the local strain rate, which can be calculated from the resolved variables, S_{ij} is the element of mean

strain rate tensor $\mathbf{S}_{ij}$, and $\tilde{S}_{ij}$ is the second-order invariant of the Favre-filtered strain rate tensor $\tilde{\mathbf{S}}_{ij}$, given by:

$$\tilde{\mathbf{S}}_{ij} = -\frac{1}{2}\left(\frac{\partial\tilde{\mathbf{u}}_i}{\partial x_j} + \frac{\partial\tilde{\mathbf{u}}_j}{\partial x_i}\right) \quad (10)$$

The Boussinesq hypothesis states that the momentum transfer caused by turbulent eddies can be modeled with an eddy viscosity ν_t allowing for the Reynolds stress tensor τ_{ij} to be proportional to the filtered mean strain rate tensor $\tilde{\mathbf{S}}_{ij}$, as shown by the relation of their elements in Eq. (9). Thus the eddy viscosity assumption (Boussinesq approximation) was employed in the framework of a standard, non-dynamic Smagorinsky-type model for the derivation of turbulent eddy viscosity as $\nu_t = [\min(C_s\Delta l)]^2|\tilde{S}_{ij}|$ (Smagorinsky, 1963). The Smagorinsky coefficient C_s was kept constant both in space and time. The values implemented were $C_s = 0.12$–0.17 (Gómez-Gesteira et al., 2012; Violeau, 2012), within the range of 0.1 to 0.24 proposed by Rogallo and Moin (1984). This approach gives rise, using Eq. (9), to the ultimate SPS stress tensor symmetric formulation (Lo and Shao, 2002), in discrete notation:

$$\frac{1}{\rho}\nabla_i\tau_{ij}^* = \sum_j m_j\left(\frac{\tau_i^*}{\rho_i^2} + \frac{\tau_j^*}{\rho_j^2}\right) \cdot \nabla_i W_{ij} \quad (11)$$

Please note that the tilde sign ($\sim$) represents, only for the aforementioned, filtered laminar values, e.g. of strain components. By adding the term of Eq. (11) in the right hand side of Eq. (5), the final equation of motion used in SPHysics can be written in particle notation (Dalrymple and Rogers, 2006):

$$\begin{aligned}\frac{d\mathbf{u}_i}{dt} = &-\sum_j m_j\left(\frac{\mathbf{P}_i}{\rho_i^2} + \frac{\mathbf{P}_j}{\rho_j^2}\right) \cdot \nabla_i W_{ij} + \mathbf{g} \\ &+ \sum_j m_j\left(\frac{4\nu\mathbf{r}_{ij}\nabla_i W_{ij}}{(\rho_i + \rho_j)|\mathbf{r}_{ij}|^2}\right)\mathbf{u}_{ij} \\ &+ \sum_j m_j\left(\frac{\tau_j}{\rho_j^2} + \frac{\tau_i}{\rho_i^2}\right) \cdot \nabla_i W_{ij}\end{aligned} \quad (12)$$

All the above add up to a robust turbulence closure model for the handling of the unresolved scales, below spatial (particle) discretization Δx. Moreover, to avoid unrealistic results like secondary bumps on the free surface, induced unfortunately by the SPS stress treatment, Panizzo (2004) proposed the use of Shepard density averaging filter. It ensured smoothness of free surface depiction and physicality of results, just as the XSPH approach (Eq. (6)) averages the local velocities terms. The filtering process was performed every 30 time steps (down to 0.3 ms of wave propagation), introducing re-initialization of each water particle density, while allowing simultaneous detailed representation of the highly nonlinear processes of wave breaking, like plunging, overturning, splash-ups and wave impact, according to:

$$\rho_i^{new} = \sum_j m_j\frac{W_{ij}}{\sum_j \frac{m_j W_{ij}}{\rho_j}} \quad (13)$$

2.3.2. LES-type approach with SPH

Detailed description of turbulence and LES approaches can be found in the book of Pope (2000). Basic inspiration for the SPHysics code implementation of a LES-type SPH model was the study of Lo and Shao (2002). In that framework, the principal idea was that the largest scales of motion should be resolved explicitly on the particle discretized computational domain, while the contribution of eddies or turbulent motions with length scales smaller than Δx would be computed through the SPS turbulence closure model. The fundamental concept to support the latter was the fact that a big amount of the flow energy is generally contained in macroscopic and mesoscopic length scales, while microscopic ones are not dependent on
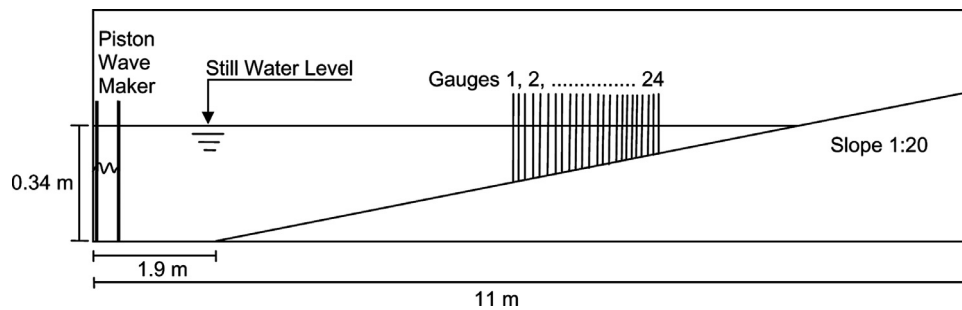
Fig. 1. Sketch of the SF05 experimental setup.

Table 1
Characteristic features of wave flume experiment (SF05).

Water depth d (m)	Flume length L_x (m)	Flume width L_y (m)	Flume depth L_z (m)	Bottom slope m_b	Wave height H (m)	Wave period T (s)	Wave breaker type	Irribaren number ξ	Ursell number Ur
0.34	11	0.3	0.6	1/20	0.105	2.42	Weak plunger	~0.4	~265

the flow and get characterized in terms of energy cascade (intermediate micro-scales) and energy dissipation (ultimate micro-scales). Thus, initially the discretization step Δx and subsequently the interparticle spacing Δl ($\mathbf{r}-\mathbf{r}'$ in vectorial notation) would support the SPH model's implicit spatial filter expressed by Eq. (1) for the decomposition of the velocity field. This is very similar to the convolution integral technique applied in LES models, as reported by various authors (Pope, 2000; Issa, 2004). However, there might be issues about the fulfillment of the presupposition that a LES approach should resolve explicitly nearly 80% of the flow etc. (Pope, 2000). Specifically, in order for the SPS-SPH model to work properly and move towards a LES-type approach, correct calibration of the spatial resolution should be completed in the first place. Therefore particle discretization Δx ought to be at least equal or better smaller than specified real flow length scales, e.g. integral turbulence ones. These could be derived from available experimental data and are discussed thoroughly below. Large turbulent or random motions, of scales above Δx values, should be resolved explicitly by the 'laminar' part of the SPH model in reasonable simulation times. Nevertheless, the need for fine spatial resolutions led to extremely large computational times for a serial (non-parallel) code, like SPHysics v.2.

3. Computational setup, pre- and post-processing techniques for SPH

The experimental data adopted for the validation of the SPS-SPH model were chosen based on two aspects. The first one was the broad variety of hydrodynamic features and processes covered by the physical simulations, in order to thoroughly validate the model's ability to capture 2-D turbulent features in the surf zone and the 2-D dynamics of weakly plunging breaking. The second one was the compact geometry of the laboratory wave flume used as a prototype domain for the numerical simulations. The latter had to do with manageable simulation times and minimization of inherent dissipative behavior of a standard SPH approach.

3.1. Experimental data

The experimental data, adopted for comparison against SPH simulations output, were collected by the physical modeling effort of Stansby and Feng (2005) [SF05 hereafter]. Their investigation covered variously the weakly plunging breaking of shore-normal nonlinear waves in a laboratory flume installation and consequent turbulence transport under them. A sketch of the flume setup is presented in Fig. 1.

The geometric and hydraulic features of the experiment are presented in Table 1. The authors reported that the regular waves started to plunge initially at about 4.95 ± 0.02 m from the wave generator, where the depth was $d\approx0.188$ m. At around 5.74 m from the wavemaker the mechanism of weak plunging had resumed full shape and the incipient breaking region ended up to this point. The breaking wave height was $H_b\approx0.169$ m and the ratio of wave height to still water depth at the breaking point was $H_b/d_b\approx0.9$ m, indicating moderate to strong nonlinearity of waves there. This was corroborated in the present study by calculating the Ursell number at the breaking point $Ur_b = H_b L_b^2 d_b^{-3}$ which was $Ur_b\approx265 \gg 100$, i.e. way larger than the limit under which linear wave theory is valid. These conditions yielded a surf similarity parameter (Irribaren number) based on the initial wave height H (in front of the wavemaker) $\xi = m_b/(H/L_0)^{1/2}$ to be about 0.46, where m_b is the bottom slope and L_0 is the theoretical deep water wave length. This value of the Irribaren number is close to 0.5, which is the boundary between spilling and plunging breakers (Battjes, 1974). The authors (SF05) stated that the waves obviously looked like they were breaking in weakly plunging form. The created water jet was almost totally reflected after hitting the forward trough. It was found that in the initial breaking phase, a cluster of nearly horizontal eddies (rotation axis parallel to the shore) was formed in the water column. Thereafter the jet re-splashed several times and generated patterns of recurring coherent vortical structures, leading to the formation of a series of horizontally elongated eddies above trough level and near the free surface.

3.2. Numerical wave tank and post-processing techniques

The size of the numerical wave tank implemented for the SPH simulations was directly correspondent to the experimental one by SF05, whose features are given in Table 1. Simulations were vertically 2-D, and comparisons with experimental output were straightforward, since all results by SF05 were presented on a vertical cross-section in the middle of the laboratory wave flume. In particular, measurements of all hydrodynamic features of interest were conducted at discrete numerical gauges in respect to the record locations of SF05. The horizontal distances x_g of the gauges from the wavemaker, as well as the respective water depth d there, are given in Table 2. In brief, gauges G1–G6 were located in the wave propagation and shoaling region, G7–G12 covered the incipient breaking and the secondary splash-up region of the plunger, G13–G19 marked the middle of the surf zone where the plunger transformed into a turbulent bore and G20–G24 were placed in the inner surf zone.

Table 2
Gauges horizontal distances from piston wavemaker (SF05).

Gauge	G1	G2	G3	G4	G5	G6	G7	G8
x_g (m)	1.094	2.404	3.404	3.904	4.404	4.904	5.304	5.540
d (m)	0.340	0.315	0.265	0.240	0.215	0.190	0.180	0.158
Gauge	G9	G10	G11	G12	G13	G14	G15	G16
x_g (m)	5.598	5.737	5.887	5.962	6.037	6.104	6.112	6.187
d (m)	0.155	0.148	0.141	0.137	0.133	0.123	0.129	0.126
Gauge	G17	G18	G19	G20	G21	G22	G23	G24
x_g (m)	6.262	6.337	6.412	6.604	6.796	7.104	7.200	7.604
d (m)	0.122	0.118	0.114	0.105	0.095	0.080	0.075	0.055

In this framework, an issue that ensued was the derivation of fluid parameters computed by a fully Lagrangian method, i.e. SPH, in an Eulerian way. The SPHysics simulations output was produced in an irregularly spaced format that followed the scattered distribution of flow particles, incommoding direct comparisons with experimental measurements on fixed locations. In order to sample the SPH fluid data on fixed nodal points, a convenient interpolation method was devised to transform the Lagrangian hydrodynamic field into an Eulerian one. This relied on the spatial averaging procedure of Farahani et al. (2012) for any arbitrary fluid parameter A_n on a fixed computational node n over its compact support domain, using the following convolution-type integral in discrete particle notation:

$$A_n = \sum_{p=1}^{N} A_p \frac{m_p}{\rho_p} W(|r_n - r_p|, h), \quad \text{for the water column}$$

$$A_n = \frac{\sum_{p=1}^{N} A_p W'(|r_n - r_p|, h)}{\sum_{p=1}^{N} W'(|r_n - r_p|, h)}, \quad \text{for free} - \text{surface boundaries}$$

(14)

where p is any neighbor particle in an area of radius r_p, around the fixed computational node n that corresponds to the exact position of the Eulerian numerical gauge and N is the total number of particles that satisfy the relation $r_p \leq h$. At the numerical gauge position, measurement points were vertically discretized by Δx. The integral kernel function could be the same with SPH method's weighting function $W(\mathbf{r}, h)$. This integration technique is justified for the computation of velocity values at fixed positions in the middle of the fluid. However, we deduced a simpler form of truncated weighted average for the interpolation of velocity at locations close to the free-surface, only when unphysical results were produced by the classic summation operator. This was done in order to avoid underestimated values due to incomplete integration. W' is a bell-shaped weighting function similar to the SPH kernel W (Eq. (3)) without the a_D factor. This method of mapping fluid data from scattered SPH particles into fixed grid nodes was basically used to compute the wave-induced currents and depth-averaged circulations, study iso-lines and/or iso-surfaces, create contour plots and slices of fluid features (Farahani et al., 2012). We hereby imposed the interpolation technique, but only at the column of vertically discretized nodes n that correspond to the Eulerian numerical gauge and not on the whole computational domain, in order to avoid extra increase of computational time.

In SF05, the LDA gauge measurements were made in order to define recurring coherent (turbulent) structures on a vertical cross-section. Velocities were point measured in such a way that the motion of monochromatic waves would allow the period-, phase- and ensemble-averaged spatial (vertical) distribution to be approximated, with coherent structures averaged over many cycles (SF05). However, instabilities of turbulent motions could render the large-scale structures not exactly repetitive. Thus the moving-average method of Nadaoka et al. (1989) was used by the authors and subsequently was implemented in the present study. The measured kinematics were therefore divided in two parts. The first was due to phase components

referring to periodic wave motion, which also include higher-order components and/or reflections from the solid boundaries in combination with repetitive coherent vortical structures. The second part was due to all residual components of turbulent motion. Interpretation of these components was further attempted through their individual Fourier spectra, yet SF05 report that it was not possible to clearly separate ensemble-averaged irrotational wave components from those due to coherent vortical structures.

In the present numerical effort of simulating a flow with abrupt transition from transient to turbulent regime, with nonlinear wave propagation, plunging breaking and bore formation, the assumption of ergodicity for the probabilistic structure of the velocity field $\mathbf{u}$ does not hold entirely. This is due to the overlapping of turbulent motions with ordered orbital motions of the wave; the overall wave motion contains both irrotational and rotational components. To discriminate accurately the rotational wave components of motion from turbulent ones is a formidable task (Nadaoka et al., 1989), because the irregular velocity components, corresponding to either turbulence or the wave itself, are superimposed reciprocally in several bands of the Fourier spectral frequency domain. Specifically the non-deterministic processes, during plunging jet splash and surface roller or bore propagation after the incipient wave breaking, lead to pattern irregularities in the underlying field. These anomalies destroy the exact repetitiveness of the overall mean periodic variations of both free surface elevation η and velocity $\mathbf{u}$ in each cycle, rendering their time series considerably different for each upcoming wave. Respective fluctuations are of the order of the wave frequency $f_w = 1/T$ and higher, especially when considering that relatively small-scale high-frequency effects are added to them (SF05) due to coherent structures. Thus a simple phase-averaging operator for the velocity field $\langle \mathbf{u} \rangle$ (Ting and Kirby, 1994, 1995) under breaking waves is not sufficient, in order to extract properly the ordered wave motion from the raw velocity u data, because the latter contain irregularly fluctuating components of both coherent structures and turbulent motions. In order to decontaminate the numerically recorded signals from residual and coherent turbulent components, we have implemented the ensemble-averaging method of Nadaoka et al. (1989). It comprises of a low-pass filter on the raw data, to remove residual turbulent components, and subsequent phase-averaging for several cycles of the low-pass filtered values of flow features, e.g. the velocity field $\tilde{\mathbf{u}}$, given by:

$$\mathbf{u}_{ens}(\mathbf{x}, \zeta t) \equiv \langle \tilde{\mathbf{u}}(\mathbf{x}, \zeta t) \rangle = \frac{1}{N} \sum_{i=0}^{N-1} \tilde{\mathbf{u}}(\mathbf{x}, \zeta (t + iT))$$

(15)

where $\langle \bullet \rangle$ is the phase-average operator, the tilde sign ($\sim$) denotes filtered values by the moving average technique, i is the sample indicator, N is the maximum sample number equal to the simulated wave cycles ($N \geq 10$), T is the wave period, ζ is the wave angular frequency, $\mathbf{x}$ is the position vector and t is the time interval of computations.

3.3. Pre-processing: turbulence flow scales vs. discretization

Before defining the test cases for validation of the SPH method, based on the most crucial calibration parameter, i.e. particle discretization Δx, analysis of the flow scales should shed some light on SPS-SPH model's potential to perform satisfactorily as a LES-type approach. The length scales of turbulent motions, vortices and eddies could be divided into three categories. The first one is the integral turbulence length scale λ_0, which corresponds to the energy containing range of the flow. This range is relevant to the large eddies which contain also a big part of the coherent vortical structures of the flow and correspond to the largest wavenumbers of the turbulence energy spectrum (Pope, 2000). These large eddy motions tap energy from the mean flow and pump it among them. Thus in this range turbulence is produced, large velocity fluctuations are manifested and high anisotropy is apparent. According to Cox et al. (1994)

Table 3
Integral turbulent length scales λ_0, with upper and lower limits Λ and Λ_{EI}, for the water column above the boundary layer threshold z_{cr} and in the middle of the boundary layer.

Gauge	d (m)	z_{cr} (m)	$z \geq z_{cr}$			$z < z_{cr}$		
			λ_o (m)	Λ (m)	Λ_{EI} (m)	λ_o (m)	Λ (m)	Λ_{EI} (m)
G8	0.1580	0.0158	0.0063	0.0379	0.0011	0.0032	0.0190	0.0005
G10	0.1482	0.0148	0.0059	0.0356	0.0010	0.0030	0.0178	0.0005
G21	0.0952	0.0472	0.0171	0.1028	0.0029	0.0094	0.0566	0.0016
G23	0.0750	0.0359	0.0135	0.0810	0.0023	0.0072	0.0431	0.0012

the mixing length is related to turbulent length scales λ_0 or characteristic eddy sizes that can be specified similarly to Deigaard et al. (1986) as:

$$\lambda_0 = \begin{cases} \kappa (z - z_0) & \text{for } z < z_{cr} = \dfrac{C_\lambda d}{\kappa} + z_0 \\ C_\lambda d & \text{for } z \geq z_{cr} = \dfrac{C_\lambda d}{\kappa} + z_0 \end{cases} \qquad (16)$$

where κ is the Von Karman constant ($\kappa \approx 0.4$), z_0 is the bottom elevation, z is the vertical distance, z_{cr} is a critical value of z which determines the bottom boundary layer, d is the local water depth, C_λ is a time-invariant empirical coefficient related to the eddy size. For the case of spilling breaking waves, Cox et al. (1994) calculated overall values of C_λ to be 0.04 outside the surf zone and at the incipient breaking region, 0.12 in the transition region at the mid surf zone and 0.18 in the inner surf zone.

The upper limit of the integral turbulence length scales is $\Lambda = 6 \cdot \lambda_0$ (Pope, 2000) and is constrained by the characteristic length of the near-shore flow. Its value was calculated to vary from 25% to 100% of the local water depth d, in the regions before or in the vicinity of the breaking point to the inner surf zone, respectively. The lower limit of the integral turbulence length scales is $\Lambda_{EI} = \lambda_0/6$ and sets the demarcation point between the anisotropic large eddies of length scales $\lambda > \Lambda_{EI}$ and the isotropic small eddies $\lambda < \Lambda_{EI}$ (Pope, 2000). Its value was found to range from 0.7% to 3% of the local water depth d, in the regions before or close to the breaking point to the inner surf zone, respectively. The calculated percentages refer to the water column outside the boundary layer ($z \geq z_{cr}$) for the specific hydraulic and geometric features of the experiment implemented (SF05). Based on Eq. (16) and the above analysis, we derived the values of λ_0, Λ, Λ_{EI}, z_{cr} on selected gauges of the numerical wave tank, presented in Table 3.

The Λ_{EI} designates the boundary between λ_0 and the Taylor microscales λ_T. The latter are the second category of turbulent flow scales, i.e. the intermediate ones between the largest and the smallest scales. They correspond to the inertial subrange of turbulence, where energy cascades to finer length scales without dissipation. Taylor microscales are often implemented as representative of the turbulent regime as they form the field of energy and momentum transfer from coarser to finer scales in the wavenumber space. The lower limit of λ_T is Λ_{DI} which discriminates them from the smallest scales in the spectrum that form the viscous sub-layer range, namely the Kolmogorov length scales λ_K. In this range, energy is dissipated due to viscosity, thus the scales involved are minuscule and correspond to high turbulent wavenumbers (frequencies) in the turbulent velocity Fourier spectrum. Turbulence is considered to be locally isotropic and homogeneous there. Taylor and Kolmogorov scales are often regarded as parts of the universal equilibrium range, which contains both the inertial sub-range and the viscous-sub layer (Pope, 2000). All the above are schematically portrayed in Fig. 2.

In the simulations of the present study, the 2-D turbulence for all scales, below either λ_0 or in the finer cases Λ_{EI}, was computed with a Smagorinsky-type SPS model. Thus similarly to a LES approach the SPS-SPH model simulated explicitly the large coherent structures in the energy containing range and modeled the intermediate and smaller ones in the inertial and dissipation ranges. Please note that there is still a long way for a complete LES implementation in SPH, e.g. explicitly simulating at least 80% of the 3-D flow and moving towards and beyond Taylor microscales. The latter implies implementing hundreds of millions of SPH particles and massively parallel simulations, even for scaled down geometries.

3.4. Calibration test cases

We followed SF05 and attempt to numerically describe the kinematics in the incipient wave breaking region (G8, G10) and the inner surf zone (G21, G23). The first region was of interest because of the intense shear and the second one due to the full development and propagation of the turbulent bore. Thus, according to Table 3, values of integral turbulence length scales λ_0, that range from 5.92 to 6.32 mm in the outer surf zone and from 1.35 to 1.71 cm in the inner surf zone, were considered to be crucial for the definition of calibration test cases, as follows. Initial particle resolution Δx should have smaller values than calculated λ_0 throughout the entire computational domain, in order to render the SPS model effective. These values were associated to the water column above the boundary layer, $z \geq z_{cr}$. The depth-averaged corresponding values for $z < z_{cr}$ were half the latter throughout the entire surf zone. The Λ_{EI} values (Table 3) are almost all smaller than 3 mm, which appeared to be the lower bound for Δx in SPHysics simulations within manageable computational times, i.e. half a month, based on the numerical setup used in the present study. In Table 4 the 2-D SPH test cases employed, based on Δx, are shown together with the corresponding number of particles N for each simulation. It is noted that the finest case with Δx equal to the lowest value of $\Lambda_{EI} = 1$ mm for $z \geq z_{cr}$ engaged nearly 1.8 million particles. To get an idea, it took nearly six months for the completion of one run with such high spatial resolution. Numerical results, based on a progressively refined discretization, were used in convergence and sensitivity analysis presented in Section 4.

The dimensionless smoothing ratio $\Delta x/h$ was taken also into account for the coarse particle spacing tests, because it could reveal optimum values. The higher the $\Delta x/h$ factor became (small smoothing length h as compared to particle resolution Δx), the more instabilities in the flow field occurred and the numerical benefits from SPH concept were enfeebled. On the other hand, low values of $\Delta x/h$ led to excessive smoothing of the flow properties and gave rise to spurious dissipative behavior by the SPH model. Thus $\Delta x/h$ ratio was defined by the c_f calibration factor which took values from 0.92 to 1.22. The lower is the one widely used in previous SPHysics studies and the higher a previously demonstrated optimum value implemented in Makris et al. (2010, 2011). Test cases 1 and 2 and 4 and 5 were characteristic examples of that. Test case 3 corresponded to a typical λ_0 value for the inner surf zone, while test cases 6–10 covered the requirements of λ_0 values for intensified shear regions such as around the incipient breaking point and the area where transition to a bore occurred. The rest cases 11–14 were endeavors to approach the lower limit of the turbulence production range $\Lambda_{EI} \approx 3 \sim 1$ mm for $z \geq z_{cr}$ (Table 3).
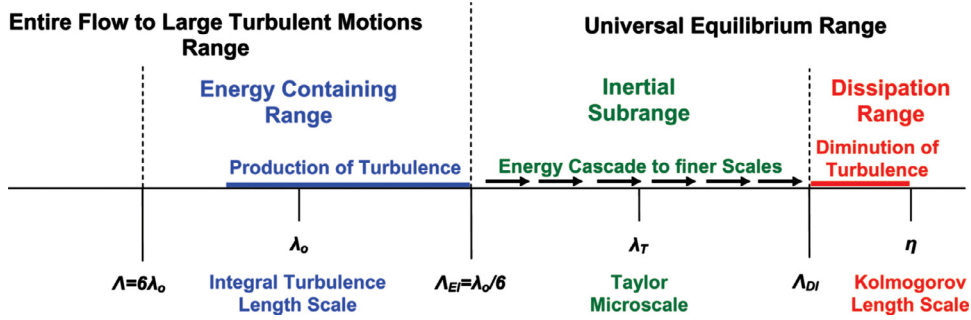
Fig. 2. Diagram of turbulent flow length scales and eddy sizes.

Table 4
Simulation test cases based on spatial resolution Δx and number of particles N.

Test case	Δx (m)	$\Delta x/h$	N	Test case	Δx (m)	$\Delta x/h$	N
1	0.02	0.77	$\sim 5 \cdot 10^3$	8	0.006	0.77	$\sim 51 \cdot 10^3$
2	0.02	0.58	$\sim 5 \cdot 10^3$	9	0.00592	0.77	$\sim 52 \cdot 10^3$
3	0.015	0.77	$\sim 9 \cdot 10^3$	10	0.005	0.77	$\sim 73 \cdot 10^3$
4	0.01	0.77	$\sim 19 \cdot 10^3$	11	0.004	0.77	$\sim 114 \cdot 10^3$
5	0.01	0.58	$\sim 19 \cdot 10^3$	12	0.003	0.77	$\sim 200 \cdot 10^3$
6	0.00632	0.77	$\sim 47 \cdot 10^3$	13	0.002	0.77	$\sim 448 \cdot 10^3$
7	0.0061	0.77	$\sim 50 \cdot 10^3$	14	0.001	0.77	$\sim 1.8 \cdot 10^6$

All simulations involved 10–50 wave periods, to ensure that sufficient data would be obtained in order to conduct analysis of turbulent features and their statistics (Cox et al., 1994). The time step Δt of simulations was chosen to be variable and reached initial values down to $\sim 1.5 \cdot 10^{-5}$ s. The sampling rate of numerical output was 100 Hz (Cox et al., 1994), thus keeping records nearly every 600 time steps. For the 50 cycles simulated, this meant $1.21 \cdot 10^4$ records of hydrodynamic features per test case and 242 records per wave period, which was considered to be adequate for the analysis of turbulent features (Nezu and Nakagawa, 1993).

4. Results

In the following, various SPH results are presented, ranging from depictions of the weakly plunging breaker and its topological particularities to comparisons against experimental (SF05) data for several wave characteristics. Representations of wave-induced currents and velocity fields covering the whole computational domain are also given, together with features of 2-D turbulence, which captures the majority of the cross-shore phenomena in the entire surf zone and gives us significant insight on the fluctuating hydrodynamic components for the energy containing range of the flow (Fig. 2).

4.1. Representation of a weakly plunging breaker

In Fig. 3 a sequence of instantaneous SPHysics results for a fine particle resolution is portrayed. The incident of weak plunging, reported by SF05, was reproduced plausibly. Initially the area below and near the wave crest transformed itself into a kind of surface roller during propagation. The roller gradually changed into an obliquely pointy bulge of water in the area of the wave crest. The latter was forced by excess in momentum to the formation of a protruding jet of water. Consequently the wave overturned, i.e. the created jet pounced and finally plunged onto the forward wave trough, impinging at the toe of the roller. This constitutes the main mechanism of vorticity generation and enhancement due to turbulent production in plunging wave breaking. The impinging tongue of water from the plunger did not penetrate the surface but pushed an adequate volume of water upfront, causing a few more resplashes. Specifically, during the first rebound splash-up, a smaller than the first tongue

was created which in turn flipped and plunged in front of the meanwhile forming turbulent bore. The latter propagated firmly creating a steep front that pushed the forward water plash into the formation of a secondary bulge shoreward of the first jet splash. Smaller than before plunging jets reappeared at the created bore front. Successive, slightly reproduced, cavities manifested themselves until the double bore subsided and transformed into ripples at the swash zone. Finer spatial discretization invoked higher quality representation of the plunger.

The color scale in Fig. 3 refers to Lagrangian 2-D velocity magnitudes $|\mathbf{u}| = \sqrt{(u^2 + w^2)}$ discretized in SPH particles form. The values of $|\mathbf{u}|$ at the propagating crest of the breaking waves and the turbulent bore fronts reached a maximum of about $|\mathbf{u}|_{max} \approx 2.9$–3.7 m/s for all simulations with $\Delta x \leq 1$ cm. A heuristic ratio of $|\mathbf{u}|_{max}$ to the theoretical shallow water celerity $c_t = (gd)^{1/2}$, namely the maximum Froude number $Fr_{max} = |\mathbf{u}|_{max}/c_t$, was calculated to be $Fr_{max} \approx 2.0$–2.6 for the incipient breaking region, gradually grew to $Fr_{max} \approx 2.2$–2.8 at the middle of the surf zone and became $Fr_{max} \approx 1.8$–3.6 in the inner surf zone. Everywhere outside the surf zone the respective ratio is $Fr_{max} < 1$, clearly indicating the regime shift from sub- to supercritical flow at the breaking point. In very shallow water, the respective ratio would instantaneously reach values of $Fr_{max} \approx 35$–50, since c_t was very low. The experimentally measured phase speed (wave celerity) c took values from $1.06 \cdot c_t$ to $1.32 \cdot c_t$ (SF05) throughout the entire surf zone. The latter was, however, close to that found by Stive (1984) for spilling and not plunging breakers. Nevertheless the maximum particle velocities $|\mathbf{u}|_{max}$, computed in the present study, were nearly 2–2.3 times higher than c in the outer surf zone and 1.4–3 in the inner surf zone. This was considered acceptable by taking into account the rapidness of the primary plunging jets during incipient breaking and the secondary tongues during bore translation, when compared to the ordered wave propagation.

Another interesting feature in Fig. 3 is the representation of four couples of detached large eddy formations during back-rush after the passing of the turbulent bore. These horizontal eddy-like structures drifted slowly offshore, towards the upcoming breaking wave, until they blended with the turbulent motions there. They reappeared and regained a coherent shape with every passing wave, having a lifespan of the order of one wave period. Besides that, the run-up in the swash zone was clearly reproduced. No further numerical treatment for the free surface coastal boundary was needed for that. However,
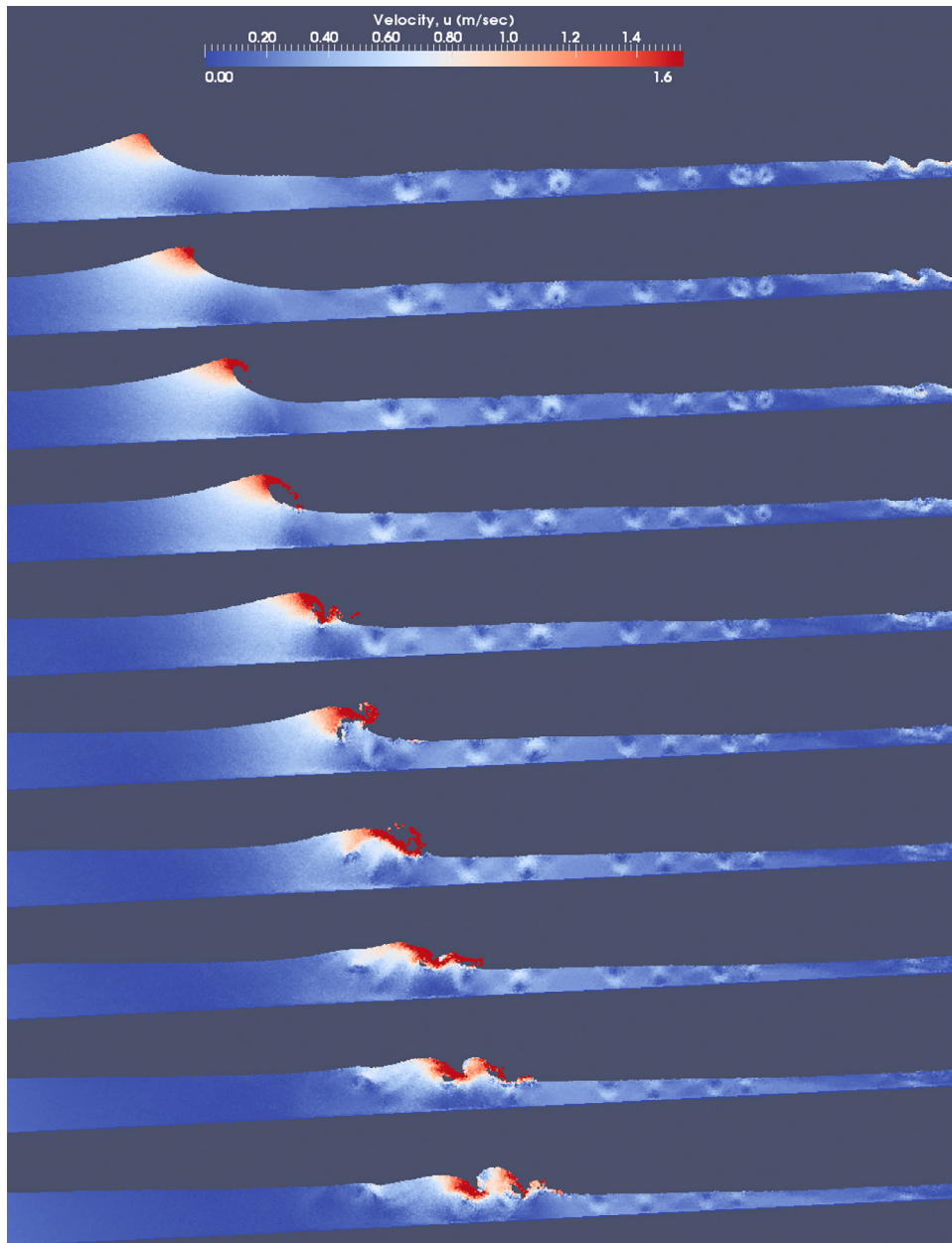
Fig. 3. Consecutive snapshots of SPHysics output for a weakly plunging breaker and consequent turbulent bore formation (test 12). Color scale corresponds to velocities and the time step of projection is 0.1 s. (For interpretation of the references to color in this figure legend, the reader is referred to the web version of this article).

friction and boundary layer treatment are still generally poor in SPH simulations.

4.2. Wave heights and set-up

The wave heights H were computed at every gauge with the use of a zero-upcrossing technique. The values of H were averaged for up to 50 wave cycles excluding measurements for the first two wave periods, which were considered to constitute a reasonable warm-up period. In Fig. 4 comparisons of experimental against numerical wave heights H and wave set-up (wave-induced mean free surface elevation) ME for low, mid, high and exceptional resolutions (upper to lower graph) are shown. For test case 1 (not shown here) values of H were reproduced well only in the wave propagation and the transition region in the mid surf zone. In spite of that, the simulations failed totally in the shoaling, breaking and inner surf zone regions. For moderate spatial resolution (test 5) comparisons were quite good, yet

simulated wave heights were not acceptable in the incipient breaking region and the inner surf zone. Initiation of plunging seemed to occur earlier than expected, namely 40 cm or at a distance equal to 12.4% of the local wave length L, before actual breaking occurred. In both 1 and 5 test cases the ME was apparently overestimated everywhere, except in very shallow waters. The wave breaking point was very well predicted, the trend of wave height evolution was plausibly reproduced and simulated values of wave heights revealed insignificant deviations from experimental ones for finer resolution (test cases 12 and 14; lower graphs of Fig. 4). Minor discrepancies were still persisting in the shear-intensified region of the plunger. The finest the resolution was the best the agreement with experimental data became for wave heights. Furthermore the wave set-up ME throughout the entire computational domain was acceptably predicted especially as resolution got refined. The set-up above the initial break point was about 10% of the wave height there and this was typical of experimental results presented by Madsen et al. (1997).
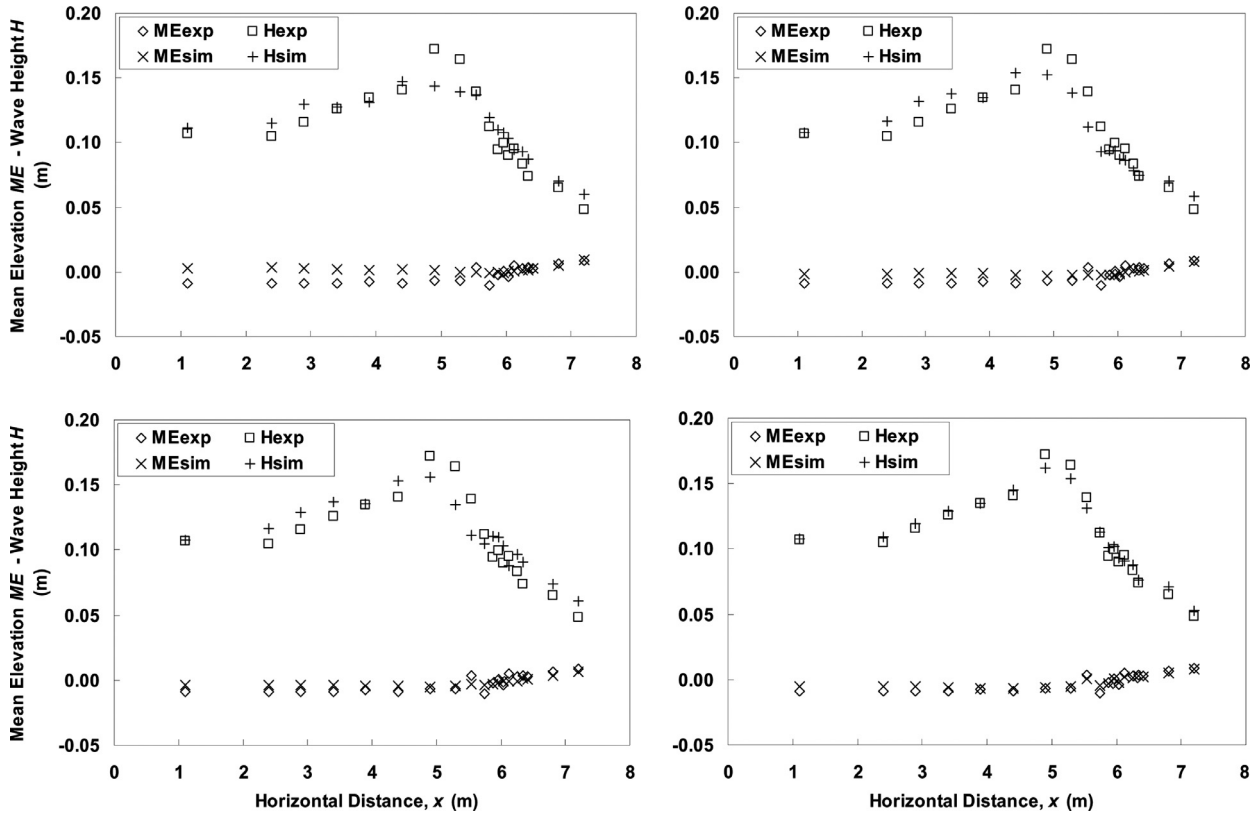
Fig. 4. Comparisons of wave height H and mean free surface elevation ME distributions between experiments (*exp*) and simulations (*sim*). From left to right and top to bottom graphs refer to test cases 5, 10, 12, and 14.

In general, agreement was plausible for wave heights H in all test cases with $\Delta x \leq 5$ mm, i.e. below integral turbulence length scale for $z > z_{cr}$. The latter was corroborated by the classic Pearson product-moment correlation for the wave height distributions by simulations against experiments. The correlation coefficient values were in the order of 0.9 for $\Delta x \leq 1$ cm and grew even higher, nearly 0.96 and 0.98 for test cases 13 and 14, respectively. The Pearson coefficient measures the strength of linear dependence between experimental and numerical data but does not compare directly their actual values. Therefore the root-mean-square error (RMSE) between experimental and numerical data was also calculated, based on the values of 18 gauges. RMSE for wave heights, H_{RMSE} (set-up, ME_{RMSE}), was 0.026 (0.014) m for test 1 and drastically decreased with increase of resolution, namely 0.012 (0.007) m, 0.013 (0.005) m, 0.01 (0.003) m and 0.005 (0.002) m for tests 5, 10, 13 and 14, respectively. Stansby and Feng (2005) state that experimental errors were in the acceptable order of 5% in their study. In our numerical study, the improvement of results based on resolution refinement, from tests 1 to 14, is of the order of 520% for H and 700% for ME. The ratios of H_{RMSE}/H_{exp} and ME_{RMSE}/ME_{exp} (H_{exp} and ME_{exp} are the experimental values of H and $|ME|$) are 15–55% and 130–3000% for test 1 reducing to 3–11% and 30–95% for test 14, respectively. It is obvious that higher SPH resolutions provide far better results than coarse ones, and that experimental errors are comparable only to RMSE of numerical wave heights for very fine resolutions (test 14). We compared also the RMSE of H and ME with initial particle spacing Δx and found that $H_{RMSE}/\Delta x$ and $ME_{RMSE}/\Delta x$ are 1.32 and 0.68 for test 1, and increase to 5.13 and 2.56 for test 14. This means that errors are somewhat in the order of the particle size for coarse resolutions, but far from comparable with Δx for fine discretization runs. Nevertheless, the free surface has been calculated based on the position of the upper particle plus half the particle's dimension, thus errors in low resolutions test cases do not rely on omission of the extent of the particle's size.

The above analysis has strong spatial differentiations, i.e. in the wave propagation and shoaling regions or in the turbulent bore region and the inner surf zone, even rather coarse spatial resolution yielded good results, especially when combined with optimum dimensionless spacing $\Delta x/h$ values. In the problematic incipient breaking region, where intense shear dominates, only fine resolution simulations gave acceptable results.

In Fig. 5, comparisons of wave crest and trough envelopes, CE and TE respectively, are presented between numerical simulations and experiments, covering the entire surf zone. Please note that the CE and TE represent the marginally higher and lower values of the free surface elevation η for the passing of all waves. A low, a moderate, and a fine spatial resolution case (from upper to lower graph; Fig. 5) are given, with acceptable agreement as Δx got smaller, especially for the trough level even in the shear intensified region of initial breaking.

4.3. Ensemble-averaged and root-mean-square wave features

The heuristic approach to analyze the flow field structure under breaking waves, rendered by Nadaoka et al. (1989), was used in the present study to define the ensemble-averaged values of several wave features (see also end of Section 3.2). The method actually consisted of applying an explicit low-pass filter on the record signals obtained from the numerical gauges. Hence, an attempt was made to reduce the contamination by the lower-frequency effects of the rotational wave components with the use of a moving-average method, where each wave cycle was divided into time-blocks. Velocities, free surface elevation, etc., were averaged for each segment of the signal. Subsequently the phase-averaging operator (Eq. (15)) was applied to each corresponding time-block, over all wave cycles of the simulation, in order to derive the aggregate mean cyclic variation (SF05). The amount of time-segments is relevant to the hydrodynamic features of interest. In the present study the large scale motions, the
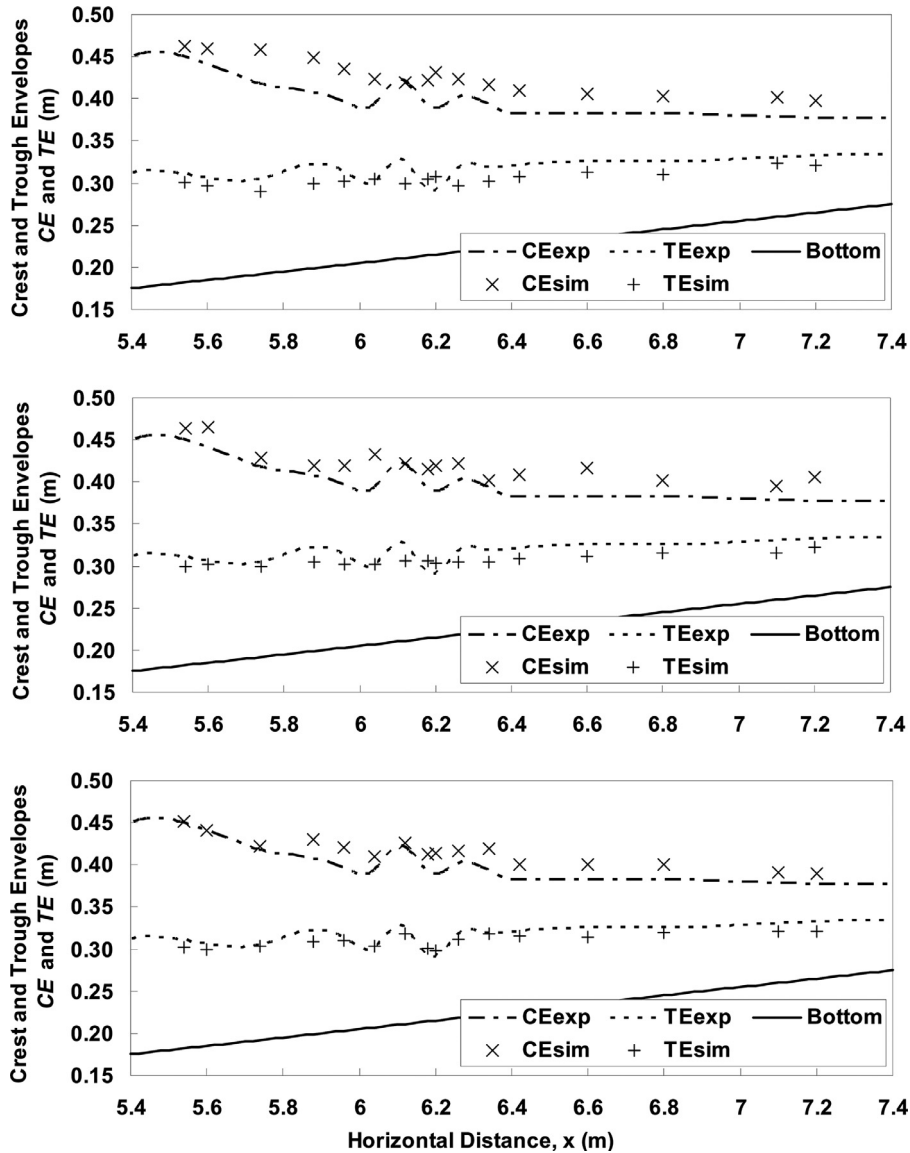
Fig. 5. Crest and trough envelopes, *CE* and *TE*, between experimental (*exp*) and simulation (*sim*) output. Tests 5, 10, and 13 from upper to lower graph presented indicatively.

recurring vortical patterns, and the coherent structures were of major importance. Consequently, the number of blocks should be large enough to define these structures. Following SF05, 121 time-blocks were implemented, which corresponded to a moving average time of 0.02 s (frequency of 50 Hz) and gave 3 samples per time-block for the sampling rate of 100 Hz. The cut-off frequency in order to fully reconstruct the initial signal or resolve the coherent turbulent structures with residual superimposed random turbulence (SF05), namely the Nyquist, limit was 25 Hz. This value corresponded to nearly 60 times the wave frequency f_w (60th harmonic). Please note that in order for the whole procedure to be successful, the time scales of turbulence should be much smaller than the wave period T. Nonetheless, for the case of wave breaking this is not always valid, as it is very hard to discriminate turbulent from ordered rotational motions due to the wave, in a transient signal produced by the propagation of the breaking wave front and the consequent turbulent bore.

In Fig. 6 comparisons of ensemble-averaged values of free surface elevation η_{ens} between experimental data and SPH simulations are presented, at specific gauges in the incipient breaking region and the inner surf zone. The best-fitted distribution of raw values, for the actual free surface elevation η in one wave period $T = 2.42$ s (*x*-axis), is

also given indicatively. Very good agreement was found covering the entire surf zone for the refined resolution tests, with $\Delta x \leq \lambda_0$. Similar comparisons are shown in Fig. 7 for the ensemble-averaged values of depth-averaged velocity U_{ens}. Results continue to be plausible at the inner surf zone, yet simulated U_{ens} was somehow underestimated at the shear intensified regions, probably due to lack of robust treatment of bottom friction and boundary layer kinematics in SPH simulations. Spatial resolution down to Taylor micro-scales ($\Delta x < \Lambda_{EI}$) should also be considered. Nevertheless, the respective raw values of U for an arbitrary wave cycle were accurate very close to the ensemble-averaged experimental data.

In the left graphs of Fig. 8 the root-mean-square (rms) values of the fluctuating free surface elevation $\eta_f = \eta_{ens} - \eta_{mean}$ (η_{mean} is the period-averaged η), are given for three refined resolution cases (10, 12 and 14 from top to bottom) at all the gauges in the surf zone. Comparisons with experimental values revealed exquisite agreement. This was also confirmed by the relevant Pearson product-moment correlation coefficients which reached very close to one, especially as spatial discretization got refined. This was not the case though for the rms depth-averaged velocity U_{rms}, as shown on Fig. 8 (right panel graphs). The relevant Pearson correlation coefficients were around
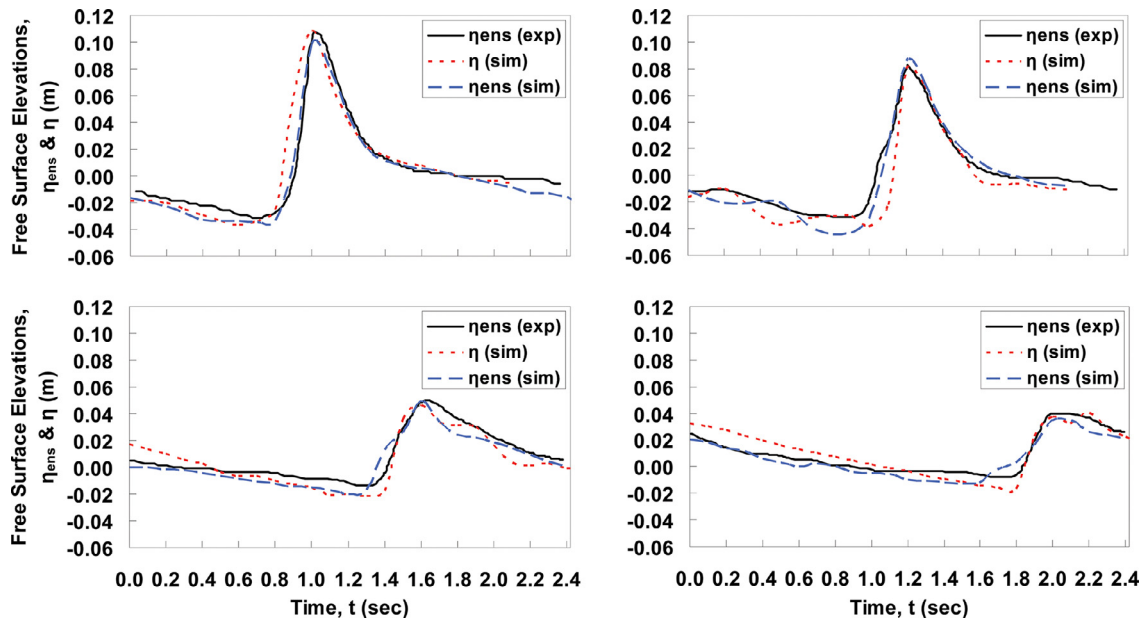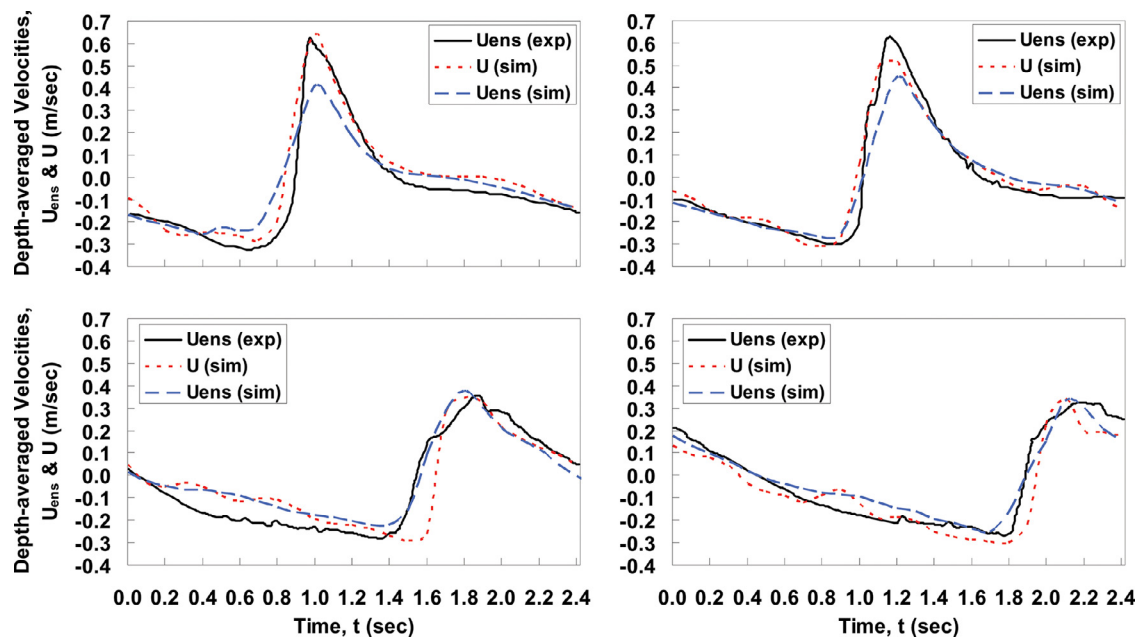
Fig. 6. Comparison of experimental (*exp*) against simulation (*sim*) data for ensemble-averaged (blue/long-dash line) and real-time (red/short-dash line) values of free surface elevation η_{ens} and η (Test 12). Upper graphs refer to G8 (left), G10 (right) at the incipient breaking region and lower graphs to G21 (left), G23 (right) at the inner surf zone. (For interpretation of the references to color in this figure legend, the reader is referred to the web version of this article).

Fig. 7. Comparison of experimental (*exp*) against simulation (*sim*) data for ensemble-averaged (blue/long-dash line) and real-time (red/short-dash line) values of depth-averaged velocities U_{ens} and U (Test 12). Upper graphs refer to G8 (left), G10 (right) at the incipient breaking region and lower graphs to G21 (left), G23 (right) at the inner surf zone. (For interpretation of the references to color in this figure legend, the reader is referred to the web version of this article).

0.5, which was somewhat dissatisfying. Nonetheless, the latter applied mostly along the transition region of the plunger to a bore in the mid surf zone, where steep water fronts were created. At the incipient breaking region or the inner surf zone comparisons with experimental data were acceptable. It is noted that the SPS-SPH model provided apparently far better results as compared to the RANS model of depth-integrated shallow water equations, used by SF05 to simulate their experiments.

4.4. Wave-induced mean flows

The investigation of surf zone hydrodynamics in this study focused also on the simulation of wave-induced mean flows. Namely the cross-shore seaward return flow (called the undertow) and the shoreward flow (broken wave mass transport added to the Stokes drift) were examined. In Fig. 9 the Eulerian period-averaged kinematics at specific gauges are portrayed, obtained from SPH results for the case of $\Delta x = \lambda_0$, covering both the whole computational domain (upper graph) and zooming in the surf zone (lower graph). The onshore current above trough level (Stokes drift) and the undertow below it were clearly visible across the wave propagation region. In the surf zone, the onshore current comprises the Stokes drift together with the broken wave's net mass transport, and the undertow is fairly larger there. These opposite wave-induced currents are clearly discerned by the calculated wave trough and crest envelopes. Another plausible attribute is the realistic depiction of the propagating wave's
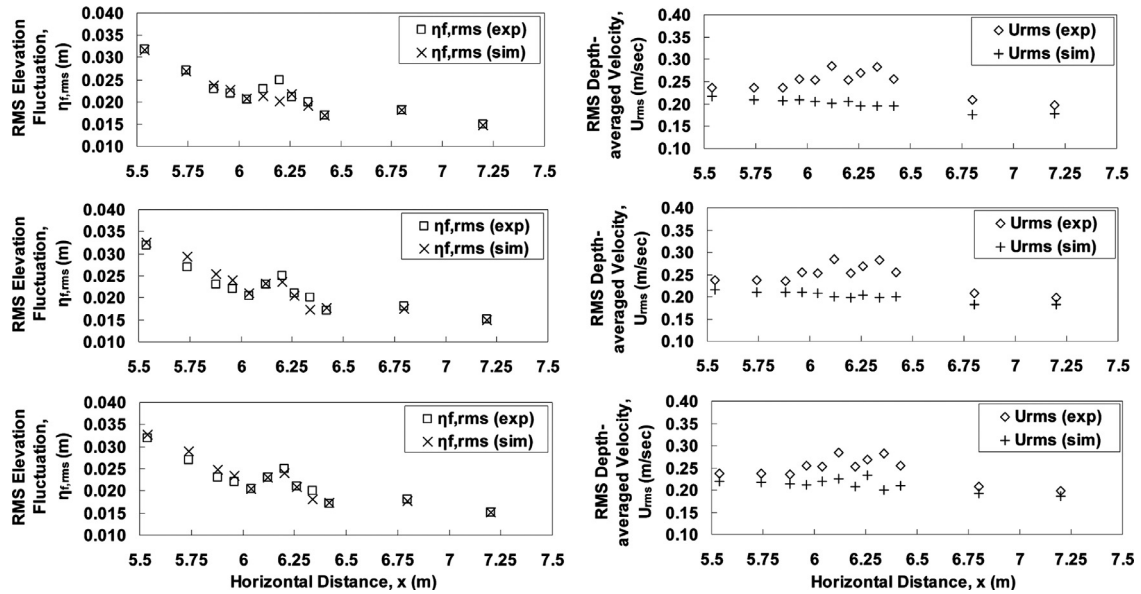
Fig. 8. Comparison of experimental (*exp*) against simulated (*sim*) rms values of free surface elevation fluctuation $\eta_{f,rms}$ (left panel) and depth-averaged velocity (right panel) for fine spatial resolution tests 10, 12 and 14 (upper, mid and lower graph respectively).
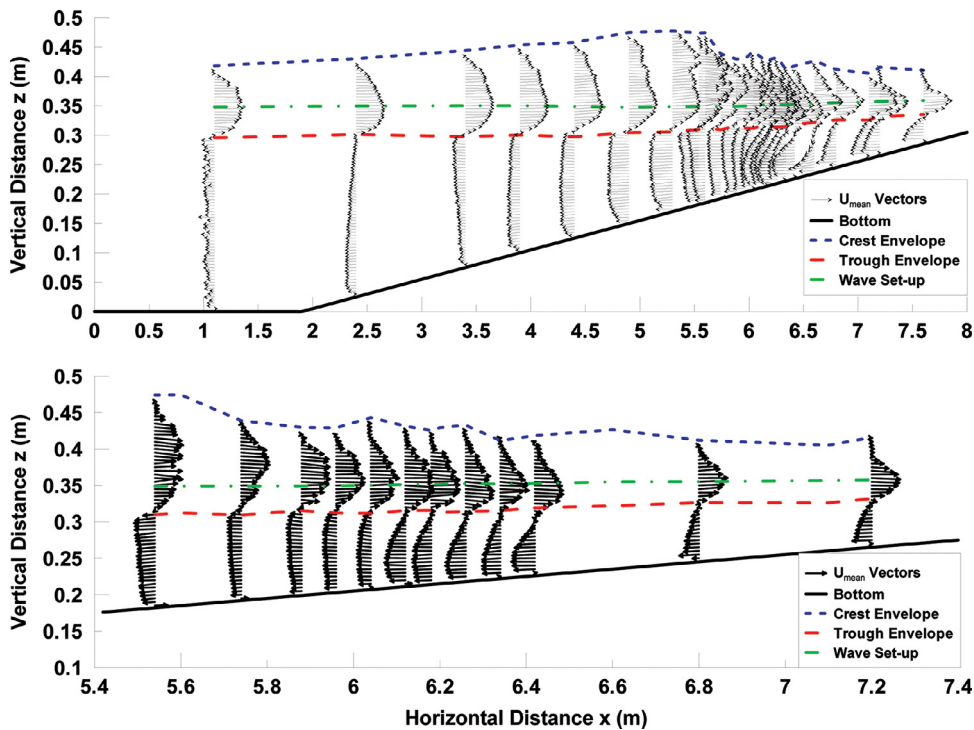

Fig. 9. Period-averaged vertical distribution of velocity vectors u_{mean} (test 10) at various gauges covering the entire computational field (upper graph) and zoomed in the surf zone (lower graph). Wave trough (red large-dash line), crest (blue small-dash line) and set-up (green dash-dot line) envelopes are shown, demarcating the undertow and shoreward drift regions. (For interpretation of the references to color in this figure legend, the reader is referred to the web version of this article).

advancing nonlinearity up to the breaking point (Fig. 9). The wave set-up level was correctly positioned between the crest and trough envelopes. The lower graph (Fig. 9) depicts the entire surf zone and reveals qualitative similarities when compared to the respective representation by SF05. Moreover, even the shoreward inversion of the mean flow near the bed, called streaming (Longuet-Higgins, 1953; Christensen et al., 2002), was reproduced qualitatively well in most cases. The latter is shown by the onshore vectors of mean velocity in the bottom boundary layer (Fig. 9), both for the propagation and the surf zone regions. This near-bed onshore current is in fact the time-average of the wave-induced oscillatory motion, which could influence significantly the shear stress distribution along the vertical near the boundary layer (Fredsøe and Deigaard, 1992). As an outcome, coherent rotational flow patterns emerged near the bed, as can be observed in vorticity maps further below.

Furthermore, in order to check the counterbalancing effect of the undertow and the shoreward drift, the depth-integrated value of mean velocity vertical distribution was calculated with the use of the
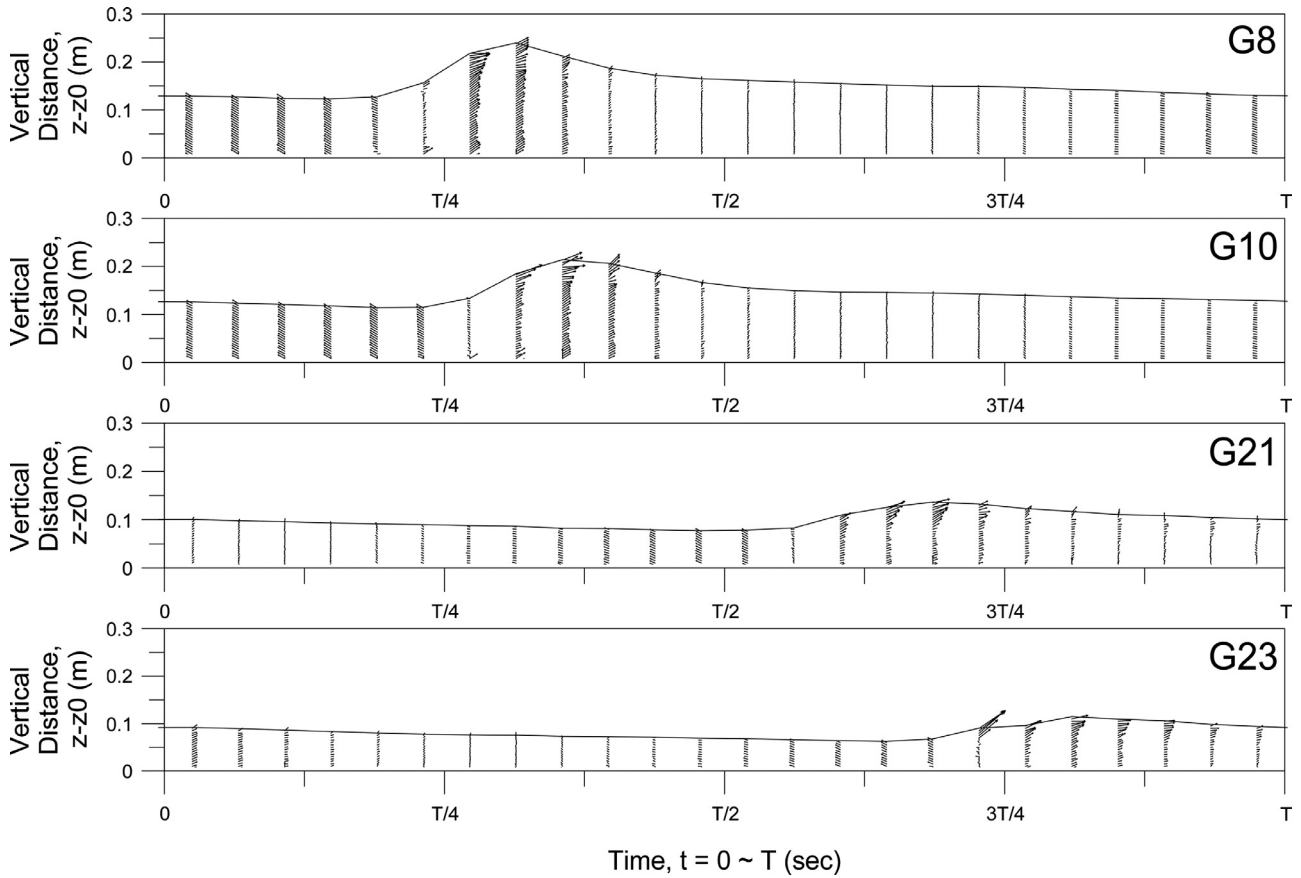
Fig. 10. Ensemble-averaged velocity u_{ens} vector plots for test 10 at the incipient breaking region G8, G10 (2 upper graphs) and the inner surf zone G21, G23 (2 lower graphs) bore region.

following relation:

$$Flux(\mathbf{u}_{mean}) = \int_{z_0}^{\eta} (\mathbf{u}_{mean})dz \qquad (17)$$

Eq. (17) actually describes the 2-D volume flux of period-averaged velocity, which was far less than 0.01 m²/s. The respective depth-averaged mean horizontal velocity U_{mean} took values almost near zero ($U_{mean} \approx 0$) in all gauges. The naught balance in shoreward and off-shore driven momentum, indicated plausible qualitative reproduction of the wave-induced mean flows throughout the entire computational domain. No need of any special treatment for the vertical distributions of the velocity field emerged for the SPH model.

Plots of simulated ensemble-averaged velocity vectors $\mathbf{u}_{ens}$ are shown in Fig. 10 for weakly plunging breakers (upper two graphs) and propagating bores (lower two graphs). Please note that the plots are against time for a whole wave period T. By comparing the velocity magnitudes against measured wave phase speed c, it was found that they were similar in the roller and the bore regions. The highest values were observed during the initiation of plunging breaking, as water jets were formed and crests overturned and the lowest values in the vicinity of the turbulent bores, probably due to their diffusive nature (SF05). The maximum velocity occurred at the wave crest above the toe of the wave in the incipient breaking region (G8 and G10) with magnitudes almost 1.5 times the measured wave celerity c. These were slightly larger than the values obtained for the initiation of spilling breakers (Qiao and Duncan, 2001). This is considered to be justifiable, by taking into account the formation of the protruding jet on the wave crest that led to the event of weak plunging. In this case the water particles are expected to have larger velocities than the case of a spilling breaker. At G21 and G23 (inner surf zone), the maximum values of numerically derived $\mathbf{u}_{ens}$ were 7–12.5% higher than c.

It is obvious that the vertical distribution of $\mathbf{u}_{ens}$ vectors was of oscillatory nature, i.e. with counterbalancing direction, during one wave cycle (Fig. 10). The pattern of the time series of $\mathbf{u}_{ens}$ vertical distributions was similar to the one of **<u>** vertical distributions in Nadaoka et al. (1989).

As a check on numerical output accuracy and following Eq. (17), the 2-D volume flux of horizontal ensemble-averaged velocity $Flux(\mathbf{u}_{ens})$ over one period was also derived, together with the respective normalized volume flux $NorFlux(\mathbf{u}_{ens})$, as shown in the formulas:

$$Flux(\mathbf{u}_{ens}) = \int_0^T \int_{z_0}^{\eta} (\mathbf{u}_{ens})dzdt$$

$$NorFlux(\mathbf{u}_{ens}) = \int_0^T \int_{z_b}^{\eta} (\mathbf{u}_{ens})dzdt \Big/ \int_0^T \int_{z_b}^{\eta} (|\mathbf{u}_{ens}|)dzdt \qquad (18)$$

It was found that $Flux(\mathbf{u}_{ens})$ was also far less than 0.01 m²/s, $Flux(\mathbf{u}_{ens}) \ll 0.01$ m²/s, and $NorFlux(\mathbf{u}_{ens})$ was calculated to be less than 5%, which was considered to be acceptably accurate and in accordance to the experimental data (SF05). The time-averaged total mass flux $Flux(\mathbf{u}_{ens})/T$, defined by Nadaoka et al. (1989), was found to be practically zero, as expected. Gradients in velocity distributions could be associated to the 2-D coherent shear and vortical structures shown further below; generally velocity gradients are linked to the wave-induced 3-D large-scale eddies in terms of a real flow. The bottom-originated vorticity also affected the vertical velocity profiles especially at the boundary layer, causing the inversion of the flow (streaming). Nonetheless the effect of boundary layer vorticity to the simulated velocity was not as important as that due to the large-scale eddies above trough level, because the bed roughness was negligibly small in the present study (SF05).
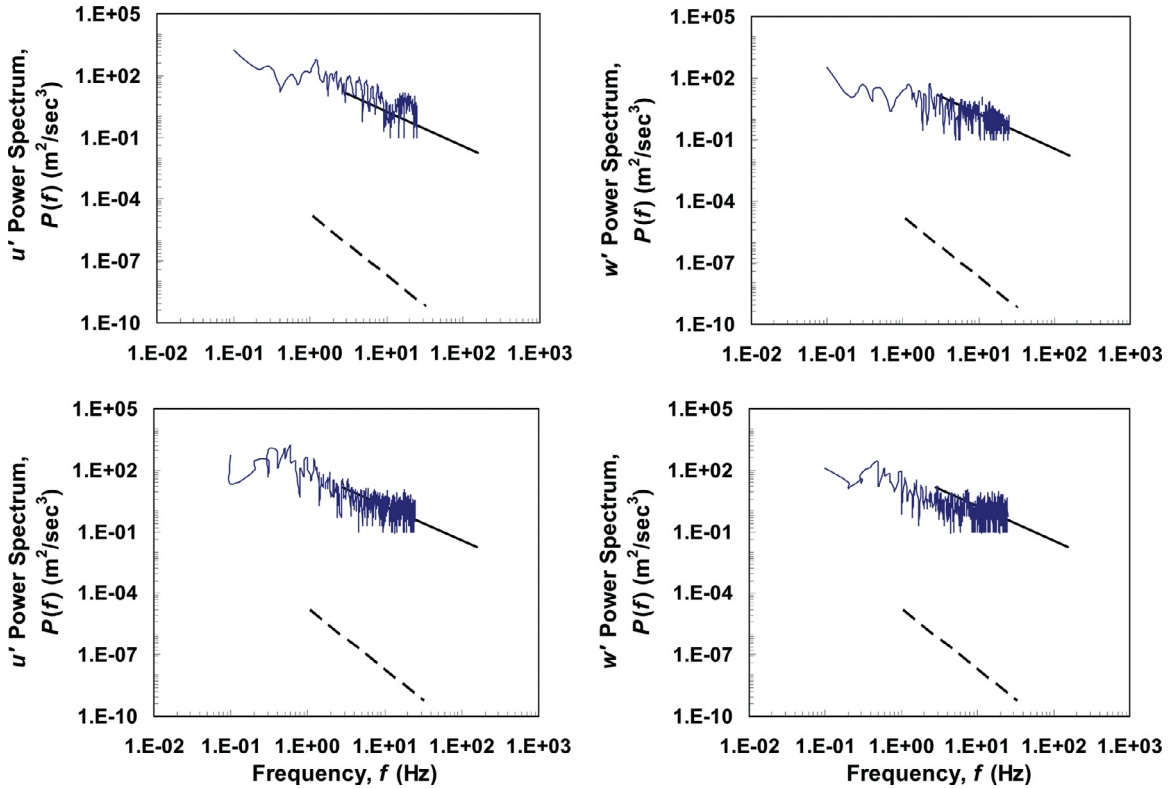
Fig. 11. Fourier spectra $P(f)$ of simulated turbulent components of horizontal u' and vertical w' velocities for the incipient breaking region (G8) [upper graphs] and the inner surf zone (G23) [lower graphs] for test 12. Measurements are taken at still water level. $-5/3$ (full line) and -3 (dash line) gradients are also shown. The Nyquist frequency was $f_N = 25$ Hz.

4.5. Fourier spectral analysis of fluctuating velocity components

LES-type simulations like those with SPS-SPH models, and more likely DNS, are the closest to experimental investigations that CFD methods could reach, especially in regard to the issue of distinguishing the turbulent fluctuations of the hydrodynamic field from the regular or ordered water motion (Christensen and Deigaard, 2001). Thus an attempt was pursued to describe the approximate turbulent features derived from 2-D SPS-SPH simulations, which are hard to obtain with the use of classic wave models. Specifically, the power spectrum of the fluctuating (approximate turbulent in 2-D) components of the Eulerian velocity field $\mathbf{u}'$ was derived. This was achieved through discrimination of the ensemble-averaged components $\mathbf{u}_{ens}$ (Eq. (15)) from the raw velocity field $\mathbf{u}$, obtained by high sampling rate numerical records, following the relation:

$$\mathbf{u}'(\mathbf{x}, \zeta t) = \mathbf{u}(\mathbf{x}, \zeta t) - \langle \tilde{\mathbf{u}}(\mathbf{x}, \zeta t) \rangle \tag{19}$$

Fig. 11 shows the Fourier power-law spectra $P(f)$ (f is the frequency) for simulated turbulent components of horizontal u' (left panel) and vertical w' (right panel) velocities at the incipient breaking region (upper graphs) and the inner surf zone (lower graphs), regarding a marginally fine spatial resolution case (test 12). For the initial breaking phase, a trend following the $-5/3$ gradient was obvious on the log/log scale, which is typical of isotropic (inertial sub-range) turbulence (Pope, 2000). This trend extended from a frequency $f = 1$ Hz and at least up to the Nyquist filter limit $f_N = 25$ Hz. Random turbulence below this frequency was lost in the averaging process. Consequently the lower limit of the large-scale structures' life-span t_{cs} would practically be of the $O(t_{cs}) = 1$ s, while turbulent energy cascade would involve coherent structures with t_{cs} at most of the $O(t_{cs}) = 0.04$ s. Improvement of previous results on the matter based on lower spatial resolution (Makris et al., 2010, 2011) was clear for median to high frequency bands that correspond to either the SPS-treated length scales or the smallest of the resolved large motions. In the present study the higher than before spatial resolution, the

finer conditional sampling technique and the sufficient number of cycles simulated contribute positively to this upgrade in numerical results. Nevertheless issues of proper treatment of turbulence measurements still remain. For example in the inner surf zone, the SPS-SPH model did not perform plausibly in simulating the effects of isotropic (inertial sub-range) turbulence at high power spectrum frequencies $f > 10$ Hz. For high frequency bands $P(f)$ deviated from its initial $-5/3$ gradient, thus making clear that no scaling power-law was evident for the small unresolved scale motions, whose effects were supposed to be modeled by the SPS approach.

All the above were relevant to areas inside the surf zone near the still water level, where thick layers of vorticity and strong vorticity gradients were present. Throughout the rest of the water column, the spectra revealed anisotropic trends for even broader frequency band widths, namely for larger scale (coherent) structures in the flow field. In addition, the -3 gradient, typical of 2-D frozen turbulence (Lesieur, 2008), was also sketched on the graphs (as in SF05), although it was never reproduced in any gauge and depth. The authors in SF05 report that turbulence quantities obtained were only superimposed residual values of relatively high frequency, not representative of all turbulence energy. This was not exactly the case in the present study, because the ensemble-averaging technique allowed lower frequency effects to be taken into account, thus representing nearly all the approximate turbulence energy. Therefore, further analysis of the Reynolds stresses and/or TKE, quadrant analysis of turbulent intensities could confirm whether residual and overall turbulence are close to or far from isotropic.

4.6. Vorticity patterns and coherent structures

We also studied the reproduction of Lagrangian and Eulerian recurring vortical patterns and respective coherent structures. The latter can be broadly defined as repeating patterns of eddy-type motion in turbulent flows. In general, the vorticity is defined in matrix
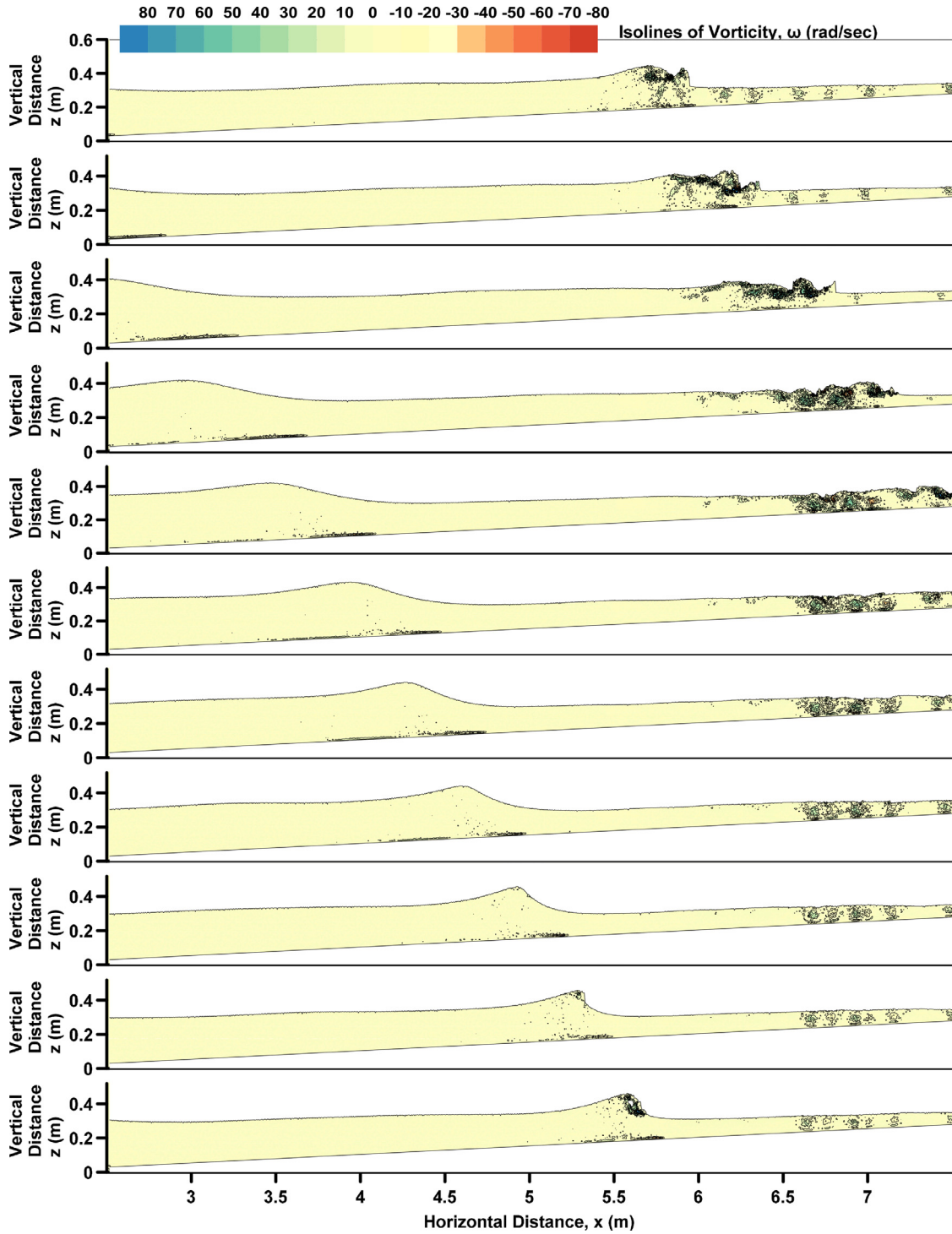
Fig. 12. Simulated vorticity field ω (s^{-1}) under weakly plunging breaking waves for test 11. Depiction of coherent structures and large scale vortical patterns for nearly one wave period (graphs equidistant at $\Delta t = 0.2$ s). (For interpretation of the references to color in this figure legend, the reader is referred to the web version of this article).

notation as $\boldsymbol{\omega} = \nabla \times \mathbf{u}$ that reads in SPH framework (Monaghan, 1992), for each arbitrary particle i and the surrounding ones j in its compact support domain, as:

$$\boldsymbol{\omega}_i = \sum_j m_j \big(\mathbf{u}_i - \mathbf{u}_j \big) \times \nabla_i W_{ij} \qquad (20)$$

For a 2-D vertical plane of the hydrodynamic field, $\boldsymbol{\omega}$ is always perpendicular to the flow and could be considered as a scalar field, given alternatively by $\boldsymbol{\omega} = \partial u/\partial z - \partial w/\partial x$.

In Fig. 12, snapshots of the ω field for one wave period are shown in a 2-D vertical cross-section; in Fig. 13 we provide enlarged regions of Fig. 12, presenting characteristic parts of it. Similar patterns of concentrated vorticity were apparent periodically, with the passage of monochromatic waves. These were coherent vortical structures involving from large-scale vortices down to small-scale eddies. It was deduced that vorticity started to gain noticeable values at the wave crest and the toe of the wavefront right before the plunging jet formation (Fig. 13a) (Peregrine and Svendsen, 1978; Zhao et al., 2004).
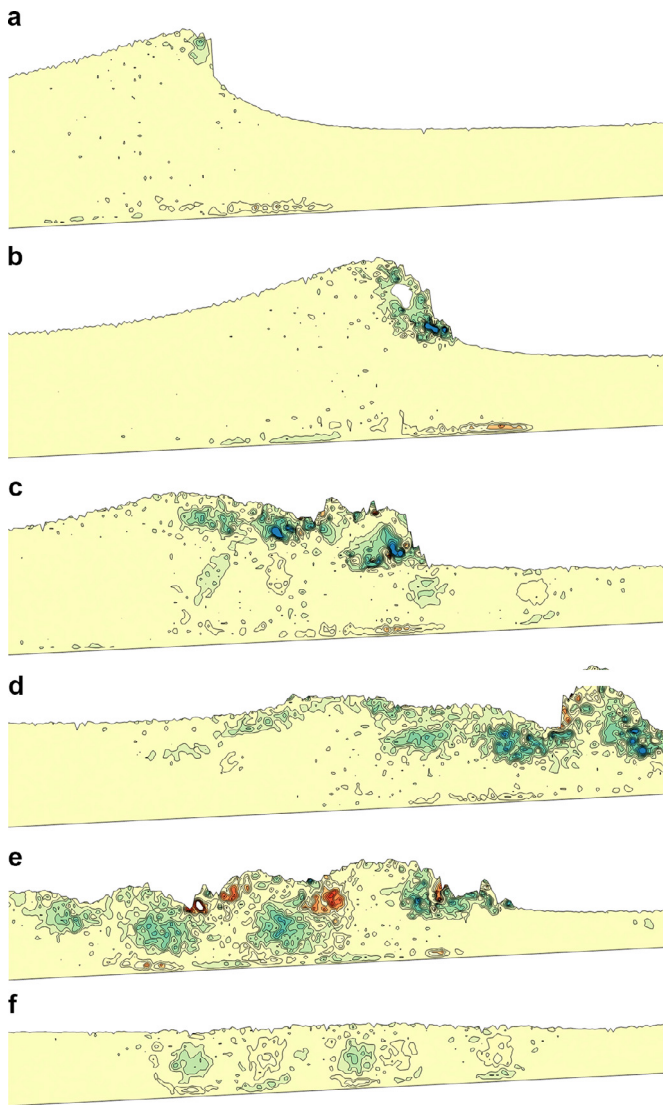
a

b

c

d

e

f

Fig. 13. Characteristic enlarged regions of coherent structures and large scale vortical patterns of the snapshots given in Fig. 12 due to simulated vorticity field ω (s^{-1}) under weakly plunging breaking waves for test 11. Contour colors correspond to the color scale in Fig. 12. a) before plunging, b) incipient plunging jet, c) permeated structures near the surface during bore propagation, d) horizontally stretched structures, e) vertical convection with blending of negative and positive vortical structures and f) residual structures. (For interpretation of the references to color in this figure legend, the reader is referred to the web version of this article).

The concentrated in this way vorticity spread out over the whole surface roller region after the initiation of the plunging breaking process. Subsequently, the impingement of the plunger on the forward trough induced the generation of topological vorticity independent of the wave-induced rotational flow (Fig. 13b). This meant that a sudden burst of vorticity took place and confined multiple vortical structures became apparent; a small part of them was descending obliquely to the bottom spreading also vorticity in the water column for a brief period after plunging (Fig. 13c). The larger part of the vortices was permeated near the free surface, seaward of the broken wave crest (Fig. 13c). This might be considered to be the end of the plunging region and the start of bore formation and propagation. During the latter coherent vortical structures were initially stretched horizontally (Fig. 13d), just as reported by SF05. Eventually they were convected vertically along the entire water column, resulting in the formation of discrete large coherent structures in the bore region and upstream of it (Fig. 13e). Anywhere else the flow was nearly irrotational, except in the region upstream of the plunger, where coherent structures short-
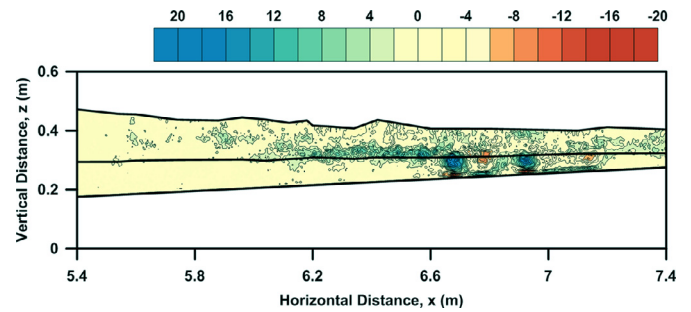

Fig. 14. Simulated period-averaged vorticity field $\bar{\omega}$ (s^{-1}) in the surf zone under weakly plunging breaking waves for test 11. Full lines show crest and trough trajectories and bottom elevation. (For interpretation of the references to color in this figure legend, the reader is referred to the web version of this article).

ened in size and torpid residual vorticity of low values was observed (Fig. 13f), due to the passage of previous breakers (also shown in Fig. 3). While the whole process was evolving, a thick layer of positive vorticity (clockwise rotations) from the free surface to trough level was evident whereas a thin layer of negative vorticity (counterclockwise rotations) prevailed at the bottom. These persisting elongated structures of negative vorticity were observed near the bed under and in front of the roller, initially similar to a mixing layer (Fig. 13b), just as shown by SF05 and Nadaoka et al. (1989). These and the formerly mentioned coherent structures in the roller region are most important in bed sediment pickup and suspension respectively, for they act as enclosed pockets that carry sediment with them, shaping its transport.

Another interesting feature was that small structures of negative vorticity merged with larger positive ones after plunging (Fig. 13e) and drifted apart in an inclined mode of about 45° following the principal axes of the mean strain rate of the phase-averaged velocity field under and behind the broken wave crest (Fig. 13c and e). This nearly $\pi/4$ tilt almost coincided with the axis of the obliquely descending eddies (Nadaoka et al., 1989) seaward of the plunging wave crest, before the coverage of a large region of the water body by coherent vortical structures. Only a 3-D representation of the flow field with really fine resolution ($\Delta x \ll 1$ mm) would enlighten the matter, although respective preliminary results seemed promising. The 3-D cases of plunging breakers simulated by other SPH researchers (Farahani et al., 2014) were not able to reproduce ODEs, yet their spatial resolution ($\Delta x = 7$ mm) probably was too coarse for this kind of analysis.

The simulated period-averaged vorticity field of a fine resolution test case is presented in Fig. 14, for the surf zone region. Please note that the axes in Fig. 14 are distorted, meaning that the actual structures presented are much more elongated. A thick layer of mean clockwise vorticity was traced in the vicinity of the wave trough level at the end of the initial breaking region, as reported also in SF05. A successive pattern of positive and negative concentrated vorticity was apparent at trough level in the bore region, followed by counterrotative structures near the bed. For the initial breakers, the maximum observed raw vorticity ω_{max} in our simulations was of the order of 10 times the maximum value of the mean vorticity $\bar{\omega}$ field, both for clockwise and counter-clockwise values. Nevertheless, this ratio was of the order of 5 over the larger part of the wave cycle. The horizontal length scale of the period-averaged coherent vortical structures, contained in the two aforementioned discrete regions, were 22–24% of the local wave length ($L_{vort} = 22$–$24\% \cdot L$) or 4.5 to 6.5 times the local water depth ($L_{vort} = 4.5$–$6.5 \cdot d$).

Simulated ensemble-averaged vorticity ω_{ens} contour plots are shown in Fig. 15 (left graphs: incipient breaking and transition regions; right graphs: middle and inner surf zone). Images of ω_{ens} refer to numerical measurements of the 2-D vorticity field evolution in time at discrete fixed (Eulerian) gauges, which was
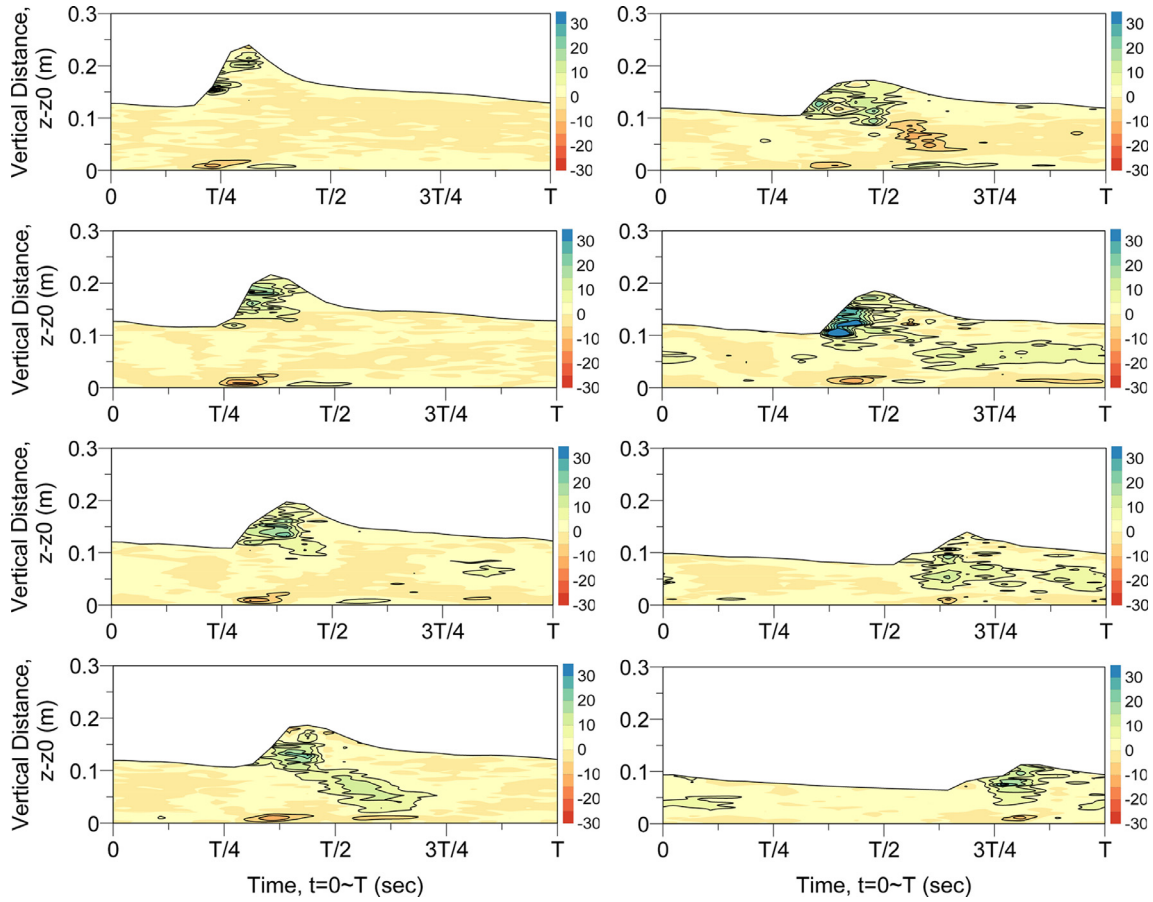
Fig. 15. Simulated ensemble-averaged vorticity ω_{ens} (s^{-1}) for weakly plunging breaking waves of test 11; from top to bottom at gauges G8, G10, G11, G12 (initial surf zone; left graphs), and gauges G13, G15, G21, G23 (middle and inner surf zone; right graphs). (For interpretation of the references to color in this figure legend, the reader is referred to the web version of this article).

derived using the method proposed in Section 3.2 and commented in Section 4.3. In general it could be said that concentrated vorticity was apparent, manifested as multiple coherent structures, at the initial breaker point, the surface roller region and the region where the plunger transformed into a bore. In the bore region those structures were evidently spread mainly horizontally. They formed a recurring pattern and could be characterized as coherent by taking into account that the vorticity field has been ensemble-averaged for up to 50 wave cycles. In particular, vorticity was generated during the initiation of breaking at G8 and G10, where positive (clockwise) values of ω_{ens} were traced near the crest and negative (anticlockwise) values of ω_{ens} near the bottom below the crest. These structures seemed to have a lifespan t_{cs} of a fraction of the wave period, around $t_{cs} = T/8 \approx 0.3$ s. This corresponded to 30 record values for the sampling rate adopted and 15 values of the ensemble-averaged signal, enough to decompose and reconstruct the coherent structures. This observation led also to the conclusion that the u' and w' values were predominantly residual turbulence values and not heavily contaminated by random low frequency wave motions or coherent structures, at least at the incipient breaking region. Thereafter, coherent vortices were multiplied in the transitional region (at G11 and G12), where they grew in size and life-time, covering almost the entire water column for more than a quarter of the wave period, i.e. $t_{cs} > T/4 \approx 0.6$ s. The vortices were all clockwise, as sketched originally by SF05 and Nadaoka et al. (1989) (for spilling breakers), except near the bottom everywhere in the surf zone and apparently at G13, where a double coherent structure of negative vorticity inclined towards the bed was evident. The coherent structures grew in size during the secondary splash-ups and the bore formation region (G15), while they spread seaward predominantly in the

horizontal direction and gained a larger lifespan. This might be considered to be the cessation cross-section for the plunging event and the start point of bore propagation (SF05).

In the inner surf zone (at G21 and G23) vorticity patterns were enfeebled yet still multiple in numbers, with the area around and above the trough level being saturated by coherent vortical structures. These were distributed along the surface as the bore propagated to shallower water in the swash zone. For the initial breakers at G8 and G10, the maximum ensemble-averaged vorticity was about $\omega_{ens,max} = 33$ s^{-1} at the toe of the breaker, which was maintained throughout the transitional region (G11 to G13) until the endpoint of the plunging event (G15), where $\omega_{ens,max}$ reached locally the extreme of 115 s^{-1}. This rapidly reduced to about 50 s^{-1} for turbulent bores at G21 and G23 downstream of the breaker. At G15 to G23, except close to the bore crest, small coherent structures were also present in the initial stages of the mean cyclic variations, i.e. for $t = 0$–$T/4$. This was residual vorticity upstream of the incident plunger due to the passage of previous breaking waves. Eventually the maximum recorded numerical vorticity, averaged through all the simulation cycles, seemed to occur right before the coherent vortices started to markedly spread along the surface (G15–G23), as reported also in SF05.

4.7. Reynolds stresses and kinetic energy

Another interesting issue, concerning the investigation of fluctuating components of hydrodynamic features in the present study, was the derivation of the TKE and Reynolds stresses. TKE can be defined as the average kinetic energy per unit mass, $\bar{k}$ or k_{ens} for steady or transient regime of the averaged fields respectively, associated with
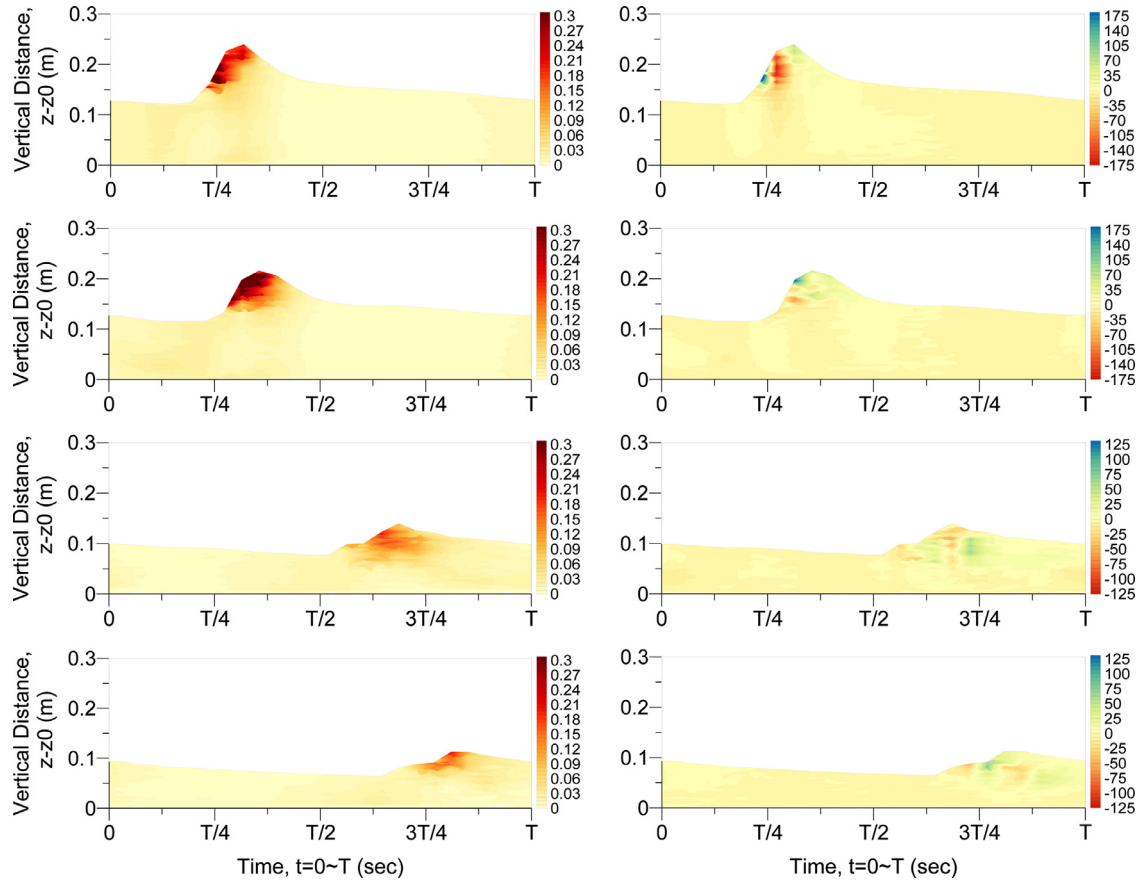
Fig. 16. Simulated ensemble-averaged 2-D TKE k_{ens} (m^2/s^2) [left graphs] and shear stress $\tau_{ss,ens}$ (Pa) [right graphs] for weakly plunging breaking waves of test 11 at the incipient breaking region and inner surf zone (from top to bottom: gauges G8, G10, G21, G23). (For interpretation of the references to color in this figure legend, the reader is referred to the web version of this article).

the eddies of the turbulent flow. In a physical sense, real-time TKE could be identified as half the numerically measured sum of mean squared velocity fluctuations (derived from $\mathbf{u}' = \mathbf{u} - \mathbf{u}_{ens}$). Therefore, it is not possible to directly reproduce snapshots of 2-D TKE for the entire computational field, due to the Lagrangian nature of the SPH method and the consequent irregularity of the particles' distribution throughout the whole domain. In order that this be feasible a background fixed grid should have been used, where the velocity field could be interpolated, above the SPS level, and the turbulent velocity fluctuations u' and w' be derived everywhere. As mentioned above, this would unduly increase the computational cost. Thus k was only calculated at fixed numerical gauges for the whole water column. In this framework, ensemble-averaged (Sections 3.2 and 4.3) values of TKE, which were associated with the large coherent 2-D cross-sections of eddies on a vertical plane of the flow (larger than Δx), were calculated based on phase-averaging of the squared numerical $\mathbf{u}'$ field (Christensen, 2006), using the following general relation:

$$k_{ens} = (\langle u'^2 \rangle + \langle w'^2 \rangle)/2 \qquad (21)$$

When the transverse horizontal turbulent velocity component v' is neglected, Eq. (21) should be multiplied by a factor of 1.33 (Stive and Wind, 1982; Svendsen 1987; Ting and Kirby, 1995) or 1.5 (Christensen, 2006), depending on the breaker type and the measurement method. These values were based on analysis of plane turbulent wakes, considered to be similar to turbulent bores in wave breaking, and could reach the value of 1.6 for natural (not laboratory) surf zones (Ruessnik, 2010). In the present case of weakly plunging regular waves, a multiplication factor of ~1.4 for Eq. (21) is used, i.e. somewhere in between the gently spilling and strong plunging cases.

Contour plots of k_{ens} in a 2-D vertical cross-section for weakly plunging breakers at fixed points in the incipient breaking region (G8, G10) and inner surf zone (G21, G23) are shown in Fig. 16 (left graphs) for rather high spatial resolution. This figure actually illustrates the temporal evolution of turbulence production and decay, during the breaking process for a wave period averaged over many cycles. Please note that if the graphs' abscissa were reversed, i.e. to denote $T-t$ as was done in SF05, and ergodicity of waves assumed (hardly the case in the highly dissipative surf zone), we could actually reproduce the ensemble-averaged wave features in spatial x-coordinate, for a wave length $x = 0-L$. Thus by careful inspection of Fig. 16 (left graphs), it can be said that 2-D TKE was produced just before breaking at the toe of the roller and took higher values on the forward front of the wave during plunging, as well as in the upper region of the undular free surface near the crest. The layers of k_{ens} were thin and dense in the initial phase of the wave passage from the fixed gauge. Afterwards, k_{ens} was diffused with time, especially when the back face of the wave was passing, thus rendering those layers sparser, thicker and of lower energy. This pattern extended from crest to trough level and was similar in both the initial and the inner surf zone. In the incipient breaking region there were also very small values of TKE in the area below the wave trough and near the bed. It was deduced that TKE was convected during the transition of the wave's undular motion from the plunger (G8 and G10) to the bore (G21 and G23). This led to a fast dissipation of TKE within one wave period, as reported also by Zhao et al. (2004). Conclusively, TKE was highest in the plunging jet region and the turbulent intensity declined immediately after the passage of the breaker. A rapid downward reduction of TKE was also obvious, suggesting that turbulence transport dominated turbulence production below trough level, as reported also by Ting and Kirby (1995).
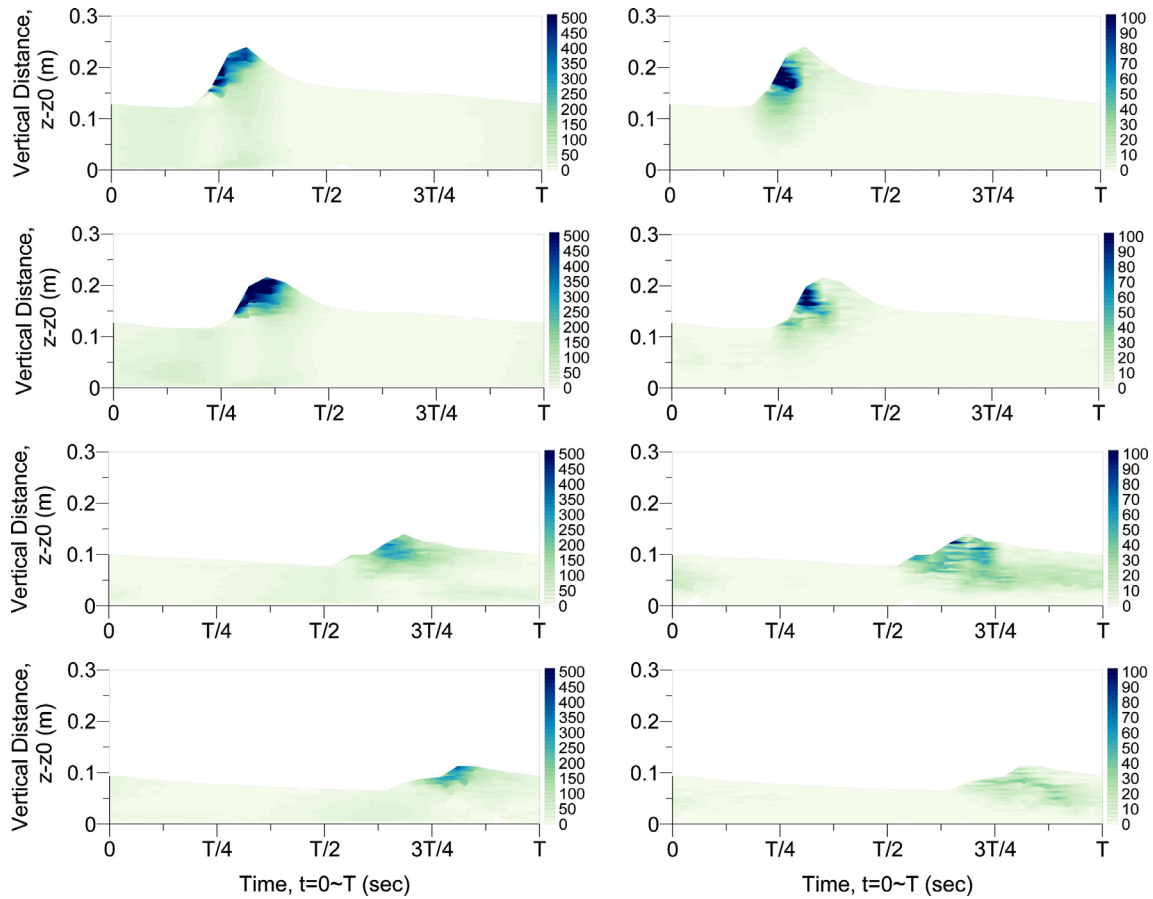
Fig. 17. Simulated ensemble-averaged horizontal and vertical normal stress $\tau_{nx,ens}$ [left graphs] and $\tau_{nz,ens}$ [right graphs] (Pa), respectively, for weakly plunging breaking waves of test 11 at the incipient breaking region and inner surf zone at gauges (from top to bottom): G8, G10, G21, G23.

Thus, unlike vorticity, no considerable amount of TKE remained behind as the wave moved into the surf zone. Therefore there were areas in the surf zone where TKE (Fig. 16, left graphs) and vorticity (Fig. 15) were not correlated. Specifically during initiation of breaking (G8), TKE coherent structures were present in the roller region near the crest, whereas coherent vortical patterns were absent there. Followingly in the region near the incipient breaking (G10), correlation of the two features was larger in spatial terms. The same patterns were also observed at the bore formation and propagation region (G21 and G23). This meant that there were considerable amounts of turbulence produced by the plunging jet without the creation of coherent vortical structures, and the residual vorticity after the passage of the wave was not accompanied by turbulence generation or conservation. Nevertheless, the reader should take into account that TKE calculated in the present study was only in reference to the large motions of the flow and not the entire TKE of the computational field. The TKE maxima of the simulated weak plunger were 0.57–0.64 m^2 s^{-2} for the incipient breaking region and 0.21–0.26 m^2 s^{-2} for the inner surf zone. These values corresponded to about 39–41% and 28–29% of the squared shallow water local celerity $c_{ts}^2 = gd$. The latter implied that the maximum levels of turbulent intensities were around 63% and 53% for the incipient breaking region and the inner surf zone, respectively. The mean TKE was 3‰ of local gd on all gauges.

Contours of simulated ensemble-averaged horizontal normal stress $\tau_{nx,ens}$ due to all turbulence in 2-D are shown in Fig. 17 (left graphs), of vertical normal stress $\tau_{nz,ens}$ in Fig. 17 (right graphs) and of shear stress $\tau_{ss,ens}$ in Fig. 16 (right graphs). These are ensemble-averaged values of Reynolds stresses that were calculated at fixed points (gauges) after the turbulent velocity components had been

defined through phase-averaging of low-pass filtered hydrodynamic features of 121 blocks per cycle. The water density was quite close to $\rho \approx 1000$ kgr/m^3 and was defined everywhere by Favre-type averaging (Section 2.3.1). It was obvious that $\tau_{nx,ens}$ took its greatest value initially at the breaking wave front (G8) and close to the crest at all remaining gauges.

The contours in Fig. 17 (left graphs) revealed that horizontal normal stresses appeared to have an almost elliptical shape in the incipient breaking region and then spread markedly as time progressed, while they appeared to be rather elongated under bores (G21 and G23). The maximum magnitudes of $\tau_{nx,ens}$ were nearly 1100–1050 Pa initially (G8–G10), which was more than two times greater than the respective value under bores with maxima in the order of 450 to 400 Pa (G21–G23). On the other hand, as presented in Fig. 17 (right graphs), $\tau_{nz,ens}$ was greatest near the toe of the breaking wave front and the roller (G8 and G10) and this continued to be the case for shallower waters also (G21 and G23) up to the ripple region where vertical normal stresses showed appreciable values only close to the surface. The contour patterns for $\tau_{nx,ens}$ were more elliptical in the initial surf zone and they became highly elongated for bores. However, they seemed to have different spatial distribution near the crest as compared to the $\tau_{nx,ens}$ contours. This indicated anisotropy of turbulence, reported also in SF05. The maximum values of vertical normal stresses were less than for horizontal ones, namely 300–190 Pa for the outer surf zone (G8–G10), which decayed rapidly in almost half to a quarter of it, 160–80 Pa, for the bore region in the inner surf zone (G21–G23).

The shear stresses, shown in Fig. 16 (right graphs), took also their extremes at the toe and the middle of the breaking wave front, with values ranging from −260 to 410 Pa. The maxima were obviously less

than the normal stresses, as reported also in SF05. In the bore region, the respective values dropped to less than half of the initial ones, with magnitudes of about −170 to 185 Pa, but with small background magnitudes residing over the entire bore front, crest and back region. One could deduce that the Reynolds stresses distribution appeared to have a peak value in the lower part of the coherent structure, i.e. at the wave trough level, where large amounts of vorticity were concentrated. This was consistent with the findings of Nadaoka et al. (1989), who described the mechanism of the instantaneous Reynolds stresses production, due to the downward motion of high velocity fluid during wave breaking within the region of eddies near the wave trough.

5. Discussion

In this study, apart from classic wave hydrodynamics in the surf zone we focused on coherent structures in a 2-D vertical plane. In that framework, temporal resolution up to around the 60th harmonic of the wave frequency was necessary. This corresponded to the Nyquist filter frequency or to turbulent motions with a lifespan of 0.04 s. By applying the moving-average method with 121 period divisions, it was implied that random turbulence below the 60th harmonic would be lost. Nevertheless the ensemble-averaging method, i.e. a combination of filtering with the phase-averaging technique over 50 wave cycles, allowed us to distinguish residual turbulence from larger coherent structures down to harmonics lower than the 60th and somehow decontaminate the ordered wave motion from large eddies. This was supported by the fact that rough −5/3 gradients (in log/log scale) of the turbulent velocity spectra followed a trend down to the second harmonic. The latter corresponded to turbulent motions and possibly large eddies with duration of nearly $T/2$. The spatial distribution of the Reynolds stresses revealed anisotropy of 2-D turbulence, in spite of the relatively high frequency cut-off compared to previous numerical studies.

In other past studies plain phase-averaging has been employed, but led to overlapping of turbulence with the wave-induced rotational motions and the coherent vortical structures. Thus the ensemble-averaging technique by Nadaoka et al. (1989) was implemented in the present study in order to discriminate wave components from coherent structures and residual turbulence. All numerical data were ensemble-averaged for several wave periods after quasi-steady state was reached, in order to improve the statistics. In this framework, the Fourier spectral gradients for the turbulent velocities, although close to −5/3, certified that numerically extracted turbulence contained also coherent structures. Therefore a clear and rigorous definition of turbulence was not possible just by using single-point Eulerian velocity measurements. Nevertheless the coherent vortical structures on a 2-D plane were plausibly reproduced and the diversity of their length scales was derived. In the weakly plunging process examined, they were generated during the initial stages of breaking and resembled to those of Nadaoka et al. (1989) for spilling breakers. However, the topological characteristics of them in the inner surf zone were quite different, yet naturally similar to the experimental ones (SF05) used as a standard for simulations presented here.

To outline the weakly plunging wave breaking event, the results indicated that turbulence appeared just before the formation of the plunging jet, at the toe and the crest of the roller. Nonetheless significant amounts of it were created impulsively with the impingement of the water tongue on the shoreward wave trough. The plunging jet splash led to a kick start for turbulent kinetic energy in the volume of water in front of the rebound area. Even though the plunging tongue did not penetrate the surface, the emerging rotating structures nearly reached the bed, yet not causing expansion of 2-D turbulence over the entire water column. Subsequently, large scale structures spread horizontally below the plunger and the rest of the generated turbulence was observed during propagation of the broken wave front and the subsequently formed bore. This was mostly due to several re-splashes of smaller plunging tongues that were created during the propagation of the broken wave and actually behaved as local sources of 2-D turbulence. Vorticity was distributed over the whole water column after the passing of each breaker, although turbulent intensities appeared to have two distinct areas of manifestation, one related to the initial breaking (G8 and G10) and the other related to the resplashing of the water pushed up by the plunger (G21 and G23).

Period-averaged kinematics revealed that the shear, between the surface roller and the back-rush flow beneath it, caused intense instabilities in the vertical distribution of velocity, which in turn led to the development of a series of horizontal coherent structures. Production of 2-D turbulence was related to them, yet the topology of concentrated TKE was different from that of vortical patterns. The shift from transient to turbulent flow regime was abrupt and lasted less than a wave cycle, i.e. 2-D turbulence was almost completely dissipated after the weakly plunging event and before the passage of the following breaker.

6. Conclusions

Based on the analysis presented, the conclusions can be divided in two categories. The one concerns the validation of the SPH model's ability to sufficiently reproduce the wave breaking process and the subsequent surf zone dynamics. The other category concerns the weak plunger itself and the relevant coherent structures identified.

Regarding the model validation, a refined-resolution calibration of an SPH model was implemented, combined with a pseudo-LES approach of a Smagorinsky-type SPS technique for 2-D turbulence closure. Numerical results were compared against the experimental data of Stansby and Feng (2005). A wide range of the dynamics of near-shore nonlinear regular wave breaking in weakly plunging form on a mild impermeable slope was investigated. In order to do that, a combination of heuristic methods was proposed for the transformation of the scattered Lagrangian data of the numerical hydrodynamic field to averaged Eulerian values at fixed gauge-type locations. Very good agreement was achieved in terms of wave height distributions both at the wave propagation region and up the slope. Moreover the SPH simulations' results for wave set-up, crest and trough envelopes, ensemble-averaged and rms values of free surface elevation were satisfactory compared to the relative experimental data. This was achieved by sensitivity analysis for the spatial discretization, which led to a choice of values in the vicinity of the demarcation point between integral and inertial turbulence length scales. Thorough analysis of the flow length scales was presented and the mixing lengths of the flow were derived based on Cox et al. (1994).

Persisting discrepancies at the incipient breaking region, where intense shear dominated, suggested that even finer resolution should be pursued in the future moving towards and beyond the Taylor micro-scales. Thus spatial resolution turned out to be the most significant factor in forming realistic results for SPS-SPH, which proved to be quite similar to LES model approaches, but not actually there yet. Due to that fact, the statistics of depth-averaged velocities were not that well reproduced. However, the SPS-SPH model yielded far better results than the inviscid shallow-water equations model used by Stansby and Feng (2005), for all the flow properties examined.

Furthermore the wave-induced mean flows were qualitatively well reproduced compared to the experimental data. The vertical distribution of period-averaged velocities clearly portrayed the undertow and composite shoreward drift regions, as well as the streaming phenomenon near the bottom, without any special manipulation of the SPH model's equations. The calculated fluxes over a wave period showed a naught balance of the opposite mean flows, both for the period- and ensemble-averaged velocity field.

The 2-D fluctuating flow features inside the surf zone were also explored with the use of SPS-SPH. Fourier spectra of turbulent intensities revealed isotropy up to rather high frequencies only in shear

intensified regions such as the free surface at the incipient break-ing point. Anisotropy of 2-D hydrodynamic fluctuations was obvi-ously everywhere else in the computational domain and this was cor-roborated by the temporal evolution of the Eulerian field for the Reynolds stresses, reported also by Stansby and Feng (2005). The heuristic approach for ensemble-averaging, based on the work of Nadaoka et al. (1989), combined with the high cut-off frequency im-plemented proved to be able in reconstructing the large-scale coher-ent structures. The large-scale repetitive patterns of vorticity, traced by the SPS-SPH model, were reproduced in a satisfactory way as compared to respective experimental studies. Spatial discretization, smaller than the integral turbulence length scale, seemed to suffice for SPH simulations of coherent structures.

Concerning the weakly plunging mechanism for wave breaking, for the particular case of a 1:20 slope, the determined coherent vor-tical structures in a 2-D vertical plane were of the order of a big part of the water column to very small fractions of it. Considerable amount of vorticity was generated at the front face of the breaking waves and then it was entrained by large scale structures, into the underlying flow field, just as reported by Nadaoka et al. (1989). Vor-ticity appeared to be significant at the toe of the surface roller and gained magnitude at the steep front of the plunger as well as at the initial bore front, but reduced rapidly after, as shown in the exper-iments by Stansby and Feng (2005). The created multiple coherent vortical structures were eventually dispersed and consequently an elongated layer of vorticity became apparent close to the surface as the bore propagated. Coherent structures of anti-clockwise vorticity were also observed near the bed, both below the bore and in front of the pre-breaking roller, resembling a mixing layer similarly to what was reported in relevant physical simulations. The derived Reynolds stresses were apparently anisotropic despite the relatively high fre-quency of record sampling for a numerical approach.

Future research on the matter should focus on the reproduction of fully 3-D coherent structures, such as obliquely descending eddies and/or braid-type and horseshoe structures under weak plungers. Thus an effort to bend the extremely time-consuming computations, involving tens to hundreds of million particles, with the use of new 'parallel' versions of the SPHysics code, i.e. DualSPHysics (Crespo et al., 2011, 2015), was set as a standard prospective goal.

References

Bakhtyar, R., Barry, D.A., Bakhtiary, A.Y., Ghaheri, A., 2009. Numerical simulation of surf-swash zone motions and turbulent flow. Adv. Water Res. 32, 250–263.

Batchelor, G.K., 1974. Introduction to Fluid Dynamics. Cambridge University Press.

Battjes, J.A., 1974. Surf similarity. In: Proceedings of the 14th International Conference on Coastal Engineering. (ICCE), pp. 466–480.

Blin, L., Hadjadj, A., Vervisch, L., 2002. Large eddy simulation of turbulent flows in re-versing systems. In: Vuillermoz, P., Comte, P., Lesieur, M. (Eds.), In: Proceedings of the 1st French Seminar on Turbulence and Space Launchers. CNES-Paris, 13–14 June 2002.

Bradford, S.F., 2000. Numerical simulation of surf zone dynamics. J. Waterw. Port Coast. Ocean Eng 126 (1), 1–13.

Christensen, E.D., Deigaard, R., 2001. Large eddy simulation of breaking waves. Coast. Eng. 42, 53–86.

Christensen, E.D., 2006. Large eddy simulation of spilling and plunging breakers. Coast. Eng. 53, 463–485.

Christensen, E.D., Walstra, D.-J., Emerat, N., 2002. Vertical variation of flow across the surf zone. Coast. Eng. 45 (3–4), 169–198.

Cox, D.T., Kobayashi, N., Okayasu, A., 1994. Vertical Variations of fluid velocities and shear stress in surf zones. In: Proceedings of the 24th International Conference on Coastal Engineering. Kobe. ASCE, pp. 98–112.

Crespo, A.J.C., Gómez-Gesteira, M., Dalrymple, R.A., 2007. 3-D SPH simulation of large waves mitigation with a dike. J. Hydraul. Res. 45 (5), 631–642.

Crespo, A.J.C., Gómez-Gesteira, M., Narayanaswamy, M.S., Dalrymple, R.A., 2008. A hy-brid boussinesq-SPH model for coastal wave propagation. In: Proceedings of the 3rd SPHERIC Workshop, ERCOFTAC. Lausanne, Switzerland.

Crespo, A.J.C., Dominguez, J.M., Barreiro, A., Gómez-Gesteira, M., Rogers, B.D., 2011. GPUs, a new tool of acceleration in CFD: efficiency and reliability on smoothed particle hydrodynamics methods. PLoS One 6 (6), e20685.

Crespo, A.J.C., Domínguez, J.M., Rogers, B.D., Gómez-Gesteira, M., Longshaw, S., Canelas, R., Vacondio, R., Barreiro, A., García-Feal, O., 2015. DualSPHysics: open-source parallel CFD solver on smoothed particle hydrodynamics (SPH). Comput. Phys. Commun. 187, 204–216.

Dalrymple, R.A., Rogers, B.D., 2006. Numerical modeling of water waves with the SPH method. Coast. Eng. 53, 141–147.

Deigaard, R., Fredsøe, J, Hedegaard, I.B., 1986. Suspended sediment in the surf zone. J. Watrway. Port Coast. Ocean Eng. 112 (1), 115–127 ASCE.

Elfrink, B., Baldock, T., 2002. Hydrodynamics and sediment transport in the swash zone: a review of perspectives. Coast. Eng. 45 (3–4), 149–167.

Farahani, R.J., Dalrymple, R.A., 2014. Three-dimensional reversed horseshoe vortex structures under broken solitary waves. Coast. Eng. 91, 261–279.

Farahani, R.J., Dalrymple, R.A., Hérault, A., Bilotta, G., 2012. SPH modeling of mean ve-locity circulation in a rip current system. In: Proceedings of the 33rd International Conference on Coastal Engineering. (ICCE). Santander. ASCE.

Fatehi, R, Manzari, M.T., 2011. A remedy for numerical oscillations in weakly compress-ible smoothed particle hydrodynamics. Int. J. Numer. Methods Fluids 67, 1100–1114.

Fredsøe, J., Deigaard, R., 1992. Mechanics of coastal sediment transport. Advanced Se-ries on Ocean Engineering, 3. World Scientific, New Jersey.

Gómez-Gesteira, M., Rogers, B.D., Dalrymple, R.A., Crespo, A.J.C., Narayanaswamy, M., 2010a. User Guide for the SPHysics Code v2.0.

Gómez-Gesteira, M., Rogers, B.D., Dalrymple, R.A., Crespo, A.J.C., 2010. State-of-the-art of classical SPH for free-surface flows. J. Hydrol. Res. 48, 6–27 Extra Issue.

Gómez-Gesteira, M., Rogers, B.D., Crespo, A.J.C., Dalrymple, R.A, Narayanaswamy, M., Dominguez, J.M., 2012. SPHysics – development of a free-surface fluid solver – Part 1: theory and formulations. Comput. Geosci. 48, 289–299.

Gotoh, H., Shao, S., Memita, T., 2004. SPH-LES model for numerical investigation of wave interaction with partially immersed breakwater. Coast. Eng. J. 46 (1), 39–63.

Gotoh, H., Shibahara, T., Sakai, T., 2001. Sub-particle-scale turbulence model for the MPS method – Lagrangian flow model for hydraulic engineering. Comput. Fluid Dyn. J. 9 (4), 339–347.

Gotoh, H., Khayyer, A., Ikaria, H., Arikawa, T., Shimosako, K., 2014. On enhancement of Incompressible SPH method for simulation ofviolent sloshing flows. Appl. Ocean Res. 46, 104–115.

Issa, R., 2004. Numerical Assessment of the Smoothed Particle Hydrodynamics Grid-less Method for Incompressible Flows and its Extension to Turbulent Flows, (Ph.D. thesis). University of Manchester Institute of Science and Technology (UMIST).

Khayyer, A., Gotoh, H., Shao, S.D., 2008. Corrected Incompressible SPH method for ac-curate water-surface tracking in breaking waves. Coast. Eng. 55 (3), 236–250.

Khayyer, A., Gotoh, H., Shao, S.D., 2009. Enhanced predictions of wave impact pressure by improved Incompressible SPH methods. Appl. Ocean Res. 31 (2), 111–131.

Khayyer, A., Gotoh, H., 2011. Enhancement of stability and accuracy of the moving par-ticle semi-implicit method. J. Comput. Phys. 230, 3093–3118.

Leimkuhler, B.J., Reich, S., Skeel, R.D., 1996. Integration methods for molecular dynam-ics. Mathematical Approaches to Biomolecular Structure and Dynamics. IMA Vol-umes in Mathematics and its Applications. Springer, pp. 161–185.

Lesieur, M., 2008. Turbulence in fluids. Fluid Mechanics and its Applications, vol. 84, fourth ed. Springer.

Li, L., Dalrymple, R.A., 1998. Instabilities of the undertow. J. Fluid Mech. 369, 175–190.

Lind, S.J., Xu, R., Stansby, P.K., Rogers, B.D., 2012. Incompressible smoothed particle hy-drodynamics for free-surface flows: a generalised diffusion-based algorithm for stability and validations for impulsive flows and propagating waves. J. Comput. Phys 231 (4), 1499–1523.

Liu, G.R., Liu, M.B., 2003. Smoothed Particle Hydrodynamic: A Meshfree Particle Method. World Scientific Publishing.

Lo, E., Shao, S., 2002. Simulation of near-shore solitary wave mechanics by an incom-pressible SPH method. Appl. Ocean Res 24, 275–286.

Longo, S., Petti, M., Losada, I.J., 2002. Turbulence in swash and surf zones: a review. Coast. Eng. 45 (3–4), 129–147.

Longo, S., 2003. Turbulence under spilling breakers using discrete wavelets. Exp. Fluids 34, 181–191.

Longuet-Higgins, M.S., 1953. Mass transport in water waves. Philos. Trans. R. Soc. Lond. A 245, 535–581.

Madsen, P.A., Sorensen, O.R., Schäffer, H.A., 1997. Surf zone dynamics simulated by a Boussinesq type model. Part I. Model description and cross-shore motion of regular waves. Coast. Eng. 32, 255–287.

Makris, C.V., Krestenitis, Y.N., Memos, C.D., 2010. Sphysics code validation against a near-shore wave breaking experiment. In: Proceedings of the 5th SPHERIC Work-shop. Manchester, pp. 245–252.

Makris, C.V., Memos, C.D., Krestenitis, Y.N., 2011. Modeling of breaking wave dynam-ics, surf zone turbulence and wave-induced mean flows with the SPH Numeri-cal Method. In: Proceedings of the 5th International Short Conference on Applied Coastal Research. SCACR. Aachen.

Monaghan, J.J., 1989. On the problem of penetration in particle methods. J. Comput. Phys. 82, 1–15.

Monaghan, J.J., 1992. Smoothed particle hydrodynamics. Annu. Rev. Astron. Astrophys. 30, 543–574.

Monaghan, J.J., 1994. Simulating free surface flows with SPH. J. Comp. Phys. 110, 399–406.

Monaghan, J.J., 2005. Smoothed particle hydrodynamics. Rep. Prog. Phys. 68, 1703–1759.

Monaghan, J.J., Kos, A., 1999. Solitary waves on a cretan beach. J. Waterw. Port Coast. Ocean Eng. 125, 145–154.

Nadaoka, K., Hino, M., Koyano, Y., 1989. Structure of the turbulent flow field under breaking waves in the surf zone. J. Fluid Mech. 204, 359–387.

Nezu, I., Nakagawa, H., 1993. Turbulence in Open Channel Flows. IAHR Monograph Se-ries. CRC Press, Taylor & Francis.

Panizzo, A., 2004. Physical and Numerical Modeling of Subaerial Landslide Generated Waves, (Ph.D. dissertation). Universita Degli Studi di L'Aquila, Italy.

Peregrine, D.H., Svendsen, I.A., 1978. Spilling breakers, bores and hydraulic jumps. In: Proceedings of the 16th International Conference on Coastal Engineering. ICCE. Hamburg. ASCE, pp. 540–550.

Petti, M., Longo, S., 2001. Turbulence experiments in the swash zone. Coast. Eng. 43, 1–24.

Pope, S.B., 2000. Turbulent Flows. Cambridge University Press.

Qiao, H., Duncan, J.H., 2001. Gentle spilling breakers: crest flow-field evolution. J. Fluid Mech. 439, 57–85.

Rogallo, R.S., Moin, E., 1984. Numerical simulation of turbulent flows. Ann. Rev. Fluid Mech. 16, 99–137.

Rogers, B.D., Dalrymple, R.A., 2004. SPH modeling of breaking waves. In: Proceedings of the 29th International Conference on Coastal Engineering. ICCE. ASCE/World Scientific Press, pp. 415–427.

Ruessnik, B.G., 2010. Observations of turbulence within a natural surf zone. J. Phys. Oceanogr. 40, 2696–2712.

Shahriari, S., Maleki, H., Hassan, I., Kadem, L., 2012. Evaluation of shear stress accumulation on blood components in normal and dysfunctional bileaflet mechanical heart valves using smoothed particle hydrodynamics. J. Biomech. 45, 2637–2644.

Shao, S., 2010. Incompressible SPH flow model for wave interactions with porous media. Coast. Eng. 57, 304–316.

Shao, S.D., Gotoh, H., 2005. Turbulence particle models for tracking free surfaces. J. Hydrol. Res. 43 (3), 276–289.

Shao, S., Ji, C., 2006. SPH computation of plunging waves using a 2-D sub-particle scale (SPS) turbulence model. Int. J. Numer. Meth. Fluids. 51, 913–936.

Skillen, A., Lind, S., Stansby, P.K., Rogers, B.D., 2013. Incompressible smoothed particle hydrodynamics (SPH) with reduced temporal noise and generalised Fickian smoothing applied to body–water slam and efficient wave–body interaction. Comput. Methods Appl. Mech. Eng. 265, 163–173.

Smagorinsky, J., 1963. General circulation experiments with the primitive equations: I. The basic experiment. Mon. Weather Rev. 91, 99–164.

Stansby, P.K., Feng, T., 2005. Kinematics and depth-integrated terms in surf zone waves from laboratory measurement. J. Fluid Mech. 529, 279–310.

Stive, M.J.F., Wind, H.J., 1982. A study of radiation stress and set-up in the surf zone. Coast. Eng 6, l–25.

Stive, M.J.F., 1984. Energy dissipation in waves breaking on gentle slopes. Coast. Eng. 8, 99–127.

Svendsen, I.A., 1987. Analysis of surf zone turbulence. J. Geophys. Res. 92 (CS), 5115–5124.

Ting, F.C.K., Kirby, J.T., 1994. Observation of undertow and turbulence in a laboratory surf zone. Coast. Eng. 24, 51–80.

Ting, F.C., Kirby, J.T., 1995. Dynamics of surf-zone turbulence in a strong plunging breaker. Coast. Eng. 24 (3–4), 177–204.

Tsuruta, N., Khayyer, A., Gotoh, H., 2013. A short note on dynamic stabilization of moving particle semi-implicit method. Comput. Fluids 82, 158–164.

Violeau, D., 2012. Fluid Mechanics and the SPH Method - Theory and Applications. Oxford University Press.

Watanabe, Y., Saeki, H., 2002. Velocity field after wave breaking. Int. J. Numer. Meth. Fluids. 39, 607–637.

Watanabe, Y., Saeki, H., Hosking, R.J., 2005. Three-dimensional vortex structures under breaking waves. J. Fluid Mech. 545, 291–328.

Wei, Z., Dalrymple, R.A., Hérault, A., Bilotta, G., Rustico, E., Yeh, H., 2015. SPH modeling of dynamic impact of tsunami bore on bridge piers. Coast. Eng. 104, 26–42.

Wendland, H., 1995. Piecewiese polynomial, positive definite and compactly supported radial functions of minimal degree. Adv. Comput. Math. 4 (1), 389–396.

Xu, R., Stansby, P.K., Laurence, D., 2009. Accuracy and stability in incompressible SPH (ISPH) based on the projection method and a new approach. J. Comput. Phys. 228, 6703–6725.

Zhao, Q., Armfield, S., Tanimoto, K., 2004. Numerical simulation of breaking waves by a multi-scale turbulence model. Coast. Eng. 51, 53–80.